

# System-based prediction of maneuvering performance of twin-propeller and twin-rudder ship using a modular mathematical model

Omer Faruk Sukas\*, Omer Kemal Kinaci, Sakir Bal

Faculty of Naval Architecture and Ocean Engineering, Istanbul Technical University, TURKEY

Corresponding author e-mail: [sukaso@itu.edu.tr](mailto:sukaso@itu.edu.tr)

## Abstract

The turning circle and zigzag maneuvering performance of surface combatant, DTMB 5415 have been investigated by using system-based method. Unsteady Reynolds averaged Navier Stokes (URANS) approach is utilized to estimate hydrodynamic derivatives and hull-propeller-rudder interactions. DTMB 5415 is a twin-propeller / twin-rudder ship and there are some studies on the derivation of maneuvering coefficients in the literature but none of them took into account the propeller and rudder forces. In this study, static drift, pure yaw, combined yaw and drift, self-propulsion and rudder tests of DTMB 5415 hull have been simulated in calm and deep water condition. Bare hull PMM simulations were carried out for a fixed Froude number of  $Fr = 0.28$ , while the simulations related to rudder and propeller were performed at  $Fr = 0.25$ . Computational results were used by MMG (Maneuvering Modeling Group) model to estimate the maneuvering performance of the ship. Hydrodynamic derivatives from numerically generated forces and moment data were obtained by single-run and multiple-run methods. The results from both methods were tested in an in-house maneuvering simulation code (MANSIM) that solves for ship motions and they were compared with computed turning circle and zigzag maneuvering performances. Although it is known a priori that the multiple-run method would give better solution in overall, it was found that the single-run method can be a good alternative in some specific cases. For the zigzag and turning circle tests, the results from single-run method were found satisfactory when correct PMM test conditions were adopted.

**Keywords:** DTMB 5415; surface combatant; MMG; mathematical model; single-run method; multiple-run method; numerical PMM

## Nomenclature

### Abbreviations

RANS	Reynolds Averaged Navier-Stokes	SR	Single Run
PMM	Planar Motion Mechanism	MR <sub>L</sub>	Low-order Multiple Run
COG	Center of Gravity	FS	Fourier Series

MMG	Maneuvering Modeling Group
DFBI	Dynamic Fluid-Body Interaction
SPSR	Single Propeller/Single Rudder
SPTR	Single Propeller/Twin Rudder
TPTR	Twin Propeller/Twin Rudder

RE	Richardson Extrapolation
LCB	Longitudinal Center of Buoyancy
LCG	Longitudinal Center of Gravity
TCG	Transversal Center of Gravity
VCG	Vertical Center of Gravity

### Symbols

$o_0 - x_0y_0z_0$	Earth-fixed coordinate system
$o - xyz$	Ship-fixed coordinate system
$u, v$	Velocities in x and y axis at midship ( $m/s$ )
$r$	Yaw rate around z axis at midship ( $rad/s$ )
$\dot{u}, \dot{v}$	Accelerations in x and y axis at midship ( $m/s^2$ )
$\dot{r}$	Acceleration around z axis at midship ( $rad/s^2$ )
$U$	Ship velocity at midship, $U = \sqrt{u^2 + v^2}$ ( $m/s$ )
$U_c$	Service speed of ship ( $m/s$ )
$Fr$	Froude number (-)
$\rho$	Water density ( $kg/m^3$ )
$g$	Gravity, $g = 9.81$ ( $m/s^2$ )
$\omega$	Angular frequency of yaw motion, $\omega = 2\pi f$ ( $rad/s$ )
$f$	Oscillation frequency of yaw motion ( $1/s$ )
$\psi$	Ship heading angle ( $rad$ )
$\beta$	Ship drift angle ( $rad$ )
$\delta$	Rudder angle ( $rad$ )
$L$	Overall length of ship ( $m$ )
$L_{wl}$	Ship waterline length ( $m$ )
$B_{wl}$	Ship beam at waterline ( $m$ )
$T$	Ship draught ( $m$ )
$C_B$	Block coefficient (-)
$C_M$	Mid-section coefficient (-)
$C_P$	Prismatic coefficient (-)
$S$	Wetted surface area of ship ( $m^2$ )

$X$	Total surge force acting on ship in x axis ( $N$ )
$X_H$	Surge force due to hull in x axis ( $N$ )
$X_R$	Surge force due to rudder in x axis ( $N$ )
$X_P$	Surge force due to propeller in x axis ( $N$ )
$Y$	Total sway force acting on ship in y axis ( $N$ )
$Y_H$	Sway force due to hull in y axis ( $N$ )
$Y_R$	Sway force due to rudder in y axis ( $N$ )
$N$	Total yaw moment acting on ship around z axis ( $N$ )
$N_H$	Yaw moment due to hull around z axis ( $N m$ )
$N_R$	Yaw moment due to rudder around z axis ( $N m$ )
$I_z$	Yaw moment of inertia around z axis ( $kg m^2$ )
$m_x, m_y$	Added mass due to ship motion in x and y directions, respectively ( $kg$ )
$f(t)$	Time histories of forces and moment acting on the hull
$J_z$	Added yaw moment of inertia around z axis ( $kg m^2$ )
$u_p$	Longitudinal inflow velocity to propeller ( $m/s$ )
$t_p$	Propeller thrust deduction factor in maneuvering motions (-)
$w_{p0}$	Effective wake fraction at propeller position in straight motion (-)
$w_p$	Effective wake fraction at propeller position in maneuvering motion (-)
$n_p$	Propeller revolution ( $1/s$ )
$D_p$	Propeller diameter ( $m$ )
$K_T$	Thrust coefficient (-)
$k_0, k_1, k_2$	Propeller open water characteristics for expressing $K_T$ (-)
$J_P$	Propeller advance ratio (-)
$\beta_P$	Geometrical inflow angle to propeller in maneuvering (-)

$m$	Ship mass ( $t$ )	$x'_p, y'_p$	Non-dimensional longitudinal and lateral position of propeller from midship (–)
$x_G$	Longitudinal position of center of gravity in $o - xyz$ ( $m$ )	$F_N$	Rudder normal force ( $N$ )
$t_R$	Steering resistance deduction factor (–)	$l'_R$	Flow-straightening coefficient of yaw rate for rudder, $l'_R = l_R/L$ (–)
$a_H$	Rudder lateral force increase factor (–)	$\varepsilon$	Ratio of effective wake fraction in way of propeller and rudder (–)
$x'_H$	Non-dimensional longitudinal position of acting point of additional lateral force (–)	$\eta$	Ratio of propeller diameter to rudder span (–)
$x'_R, y'_R$	Non-dimensional longitudinal and lateral coordinate of rudder position, respectively (–)	$\kappa$	An experimental constant for expressing $u_R$ (–)
$\Lambda$	Rudder aspect ratio (–)	$A'_T$	Advance in turning maneuver (–)
$A_R$	Profile area of movable part of mariner rudder ( $m^2$ )	$T'_T$	Transfer in turning maneuver (–)
$u_R, v_R$	Longitudinal and lateral inflow velocity components to rudder, respectively ( $m/s$ )	$D'_T$	Tactical diameter in turning maneuver (–)
$\alpha_R$	Effective inflow angle to rudder ( $rad$ )	$r'_T$	Steady yaw rate in turning maneuver (–)
$\delta_R$	Effective rudder angle where the rudder normal force becomes zero ( $rad$ )	$U'_T$	Steady turning speed (–)
$\gamma_R$	Flow-straightening coefficient of sway velocity for rudder (–)	$OA_{1st}$	First overshoot angle in zigzag maneuvering ( $deg$ )
$\beta_R$	Effective drift angle at rudder position ( $rad$ )	$OA_{2nd}$	Second overshoot angle in zigzag maneuvering ( $deg$ )
$H_R$	Rudder span length ( $m$ )		

## 1. Introduction

Improving ship maneuvering performance which is directly associated with navigation safety and economy is a very important part of design process that often requires high cost and long computation times. Primary features of maneuverability, such as turning and course keeping abilities, often require contradictory design properties that makes the problem challenging to design a ship with good maneuverability in every aspect. Thus, an effective optimization study should be performed under the cost and performance constraints during the preliminary design stage.

Research in the field of ship maneuverability have been increased in recent years. Many review papers have been presented so far to highlight ship maneuverability about prediction methods (Sukas et al., 2018a,b), mathematical models (Sutulo and Soares, 2011), inland vessels (Liu et al., 2015), shallow and restricted water effects (Vantorre, 2003), and rudder performance (Liu and Hekkenberg, 2017). Some basic empirical approaches are usually preferred to estimate the maneuvering performance in the initial design stage (Kijima et al., 1990; Lee and Shin, 1998; Yoshimura and Masumoto, 2012; Liu et al., 2017). However, in some cases where further analyses are required, calculations may need to be carried out with experimental or numerical methods to obtain more precise results. Particularly, as the high performance computing has been developed in the last few decades, extensive studies have been made with computational tools such as RANS (Reynolds Averaged Navier-Stokes) to assess the maneuvering performance of ships. There are two types of RANS-based application used in maneuvering predictions such as CFD-based and system-based

methods. The first one includes full time-domain simulation of free running tests with steering rudder(s) and rotating propeller(s). Recent examples of the real-time maneuvering simulations can be found in (Shen et al., 2015; Carrica et al., 2016; Ohashi et al., 2018) for ships with single rudder configuration. Carrica et al. (2013), Moctar et al. (2014), Dubbioso et al. (2015) have also carried out full time-domain simulations for ships with twin rudder configuration. However such direct methods require enormous computational resources which restrict its feasibility for practical purposes. In system-based methods, the hydrodynamic derivatives used in the equations of motion can be obtained from numerical simulations of captive tests which are straight line test, planar motion mechanism (PMM) or circular motion test (CMT). Several studies have been carried out using RANS tools to estimate the hydrodynamic derivatives utilizing FS (Fourier Series) expansion (Sakamoto et al., 2012a; Yoon et al., 2015a; Liu and Zou, 2018). Hydrodynamic derivatives can also be estimated from free-running data or direct CFD simulation results using system identification techniques (Araki et al., 2012). Free running maneuvers can be simulated with these hydrodynamic derivatives using a mathematical model such as Abkowitz model (Abkowitz, 1964) or MMG (Maneuvering Modeling Group) model (Ogawa and Kasai, 1978; Yasukawa and Yoshimura, 2015). The latter is mostly preferred by researchers due to its modular background since it is possible to take the hull-rudder-propeller interaction into account. The original MMG model is usually used for single-propeller single-rudder (SPSR) configurations (Liu et al., 2015; He et al., 2016; Arai and Hino, 2017), but it has also been extended to single-propeller twin-rudder (SPTR) and twin-propeller twin-rudder (TPTR) cases. For instance, Kang et al. (2008) developed a mathematical model for a large SPTR ship and validated the results with free running data. The interactions of hull-propeller and hull-rudder were investigated experimentally, as well as the factors affecting the maneuvering performance of twin rudder system. Lee et al. (2003) modified the MMG model and proposed a new mathematical model for a TPTR ship, and validate the results with experimental data. Khanfir et al. (2011) proposed another method based on hill-climbing procedure to estimate the hull-rudder interaction coefficients for SPTR and TPTR ships. It was also reported that the flow-straightening coefficient shows a slight variation for starboard and port side turnings for SPSR and TPTR ships, whereas it is remarkably asymmetric for SPTR ships. Guo and Zou (2017) and Guo et al. (2018) utilized a RANS tool to obtain hydrodynamic derivatives and the interaction among the hull, propeller and rudder by investigating the local flow field in detail. Subsequently, the turning and zigzag maneuvers of a TPTR ship were simulated using a 4-DOF MMG model and the trajectories and some kinematical parameters were compared with the free running data.

In this study, the effects of different methods which are based on FS expansion for obtaining the hydrodynamic derivatives on free running simulations are investigated. Numerical simulations of static drift test, pure yaw test and yaw-drift test are carried out for the DTMB5415 model with TPTR configuration. The primary aim here is to compare the results of turning and zigzag maneuvers by single-run (SR) method with those of multiple-run ( $MR_L$ ) method. The  $MR_L$  method requires more CFD simulations than SR method. Although the  $MR_L$  method is known to be more reliable (Sakamoto et al., 2012; Yoon et al., 2015), the accuracy of the results obtained by SR method has also been investigated since it has an advantage in terms of computational time. Meanwhile, the hull-propeller and the hull-rudder interaction coefficients are predicted by performing self-propulsion, static rudder and combined drift-rudder simulations. Then, a system-based simulation of turning and zigzag maneuvers in calm and deep water condition is carried out using a 3-DOF MMG model. Predicted trajectories and time histories of kinematic parameters are compared with the available experimental data.

## 2. Mathematical Model

In this study, 3-DOF maneuvering motion for a ship with TPTR (twin-propeller, twin-rudder) configuration is numerically simulated utilizing MMG models used by Lee and Fujino (2003), Yasukawa and Yoshimura (2015) and Khanfir et al. (2011). Briefly; the model breaks the total hydrodynamic forces into different parts (contributors) from hull, rudders and propellers. The interaction effects of hull-rudders and hull-propellers are also taken into account by self-propulsion and rudder tests. The coordinate system and the equations of maneuvering motion for hydrodynamic forces and moment will be described in the following sub-sections.

### 2.1 Coordinate Systems

The basic dynamic of motion can be described using the Newton's second law of motion, hence two different coordinate systems can be defined for a maneuvering ship: earth-fixed coordinate system ( $o_0 - x_0y_0z_0$ ) and ship-fixed ( $o - xyz$ ) coordinate system as shown in Figure 1. The origin of the earth-fixed coordinate system is generally considered to be the point where the maneuvering motion starts, while the origin of the ship-fixed coordinate system is selected on the midship.

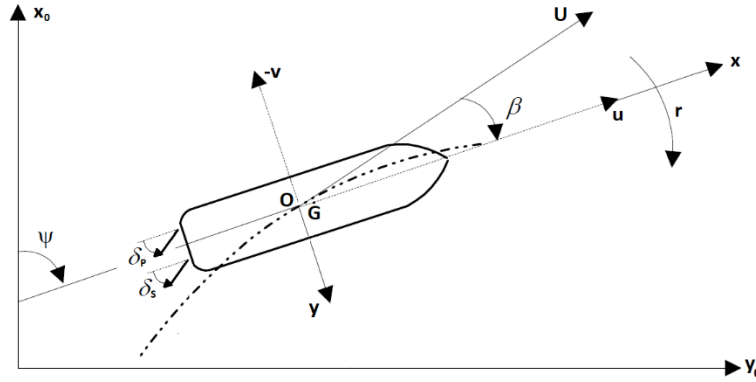


**Fig. 1.** Earth-fixed and ship-fixed coordinate systems to define 3-DOF ship maneuvering motion.

The heading angle,  $\psi$  refers to the angle between  $x$  and  $x_0$  axis. The dash-dot curve shows the trajectory of ship. The difference between ship's heading and actual course direction (velocity vector at COG) is drift angle,  $\beta = \tan^{-1}(-v/u)$ . The rudder angle,  $\delta$  is positive while rotating to starboard side.  $u$  and  $v$  denote the velocity components in  $x$  and  $y$  directions,  $r$  is yaw rate that can also be defined as  $r = \frac{\partial \psi}{\partial t}$ . The speed of ship is indicated as  $U (= \sqrt{u^2 + (-v)^2})$ .

### 2.2 Equations of Motion in Horizontal Plane

The maneuverability of a traditional ship form on the calm water surface is examined for surge, sway and yaw motions. Therefore, a basic 3-DOF model in horizontal plane is used in the calculations. The equations of maneuvering motion in ship-fixed coordinate system can then be expressed as follows (Yasukawa and Yoshimura, 2015):

$$\begin{aligned} (m + m_x)\dot{u} - (m + m_y)vr - mx_G r^2 &= X_H + X_R + X_P \\ (m + m_y)\dot{v} + (m + m_x)ur + mx_G \dot{r} &= Y_H + Y_R \\ (I_z + J_z + mx_G^2)\dot{r} + mx_G(\dot{v} + ur) &= N_H + N_R + Y_H x_G \end{aligned} \quad [1]$$

The subscripts  $H$ ,  $R$  and  $P$  refer to hull, rudder and propeller, respectively.  $m$  is the ship mass and  $I_z$  is moment of inertia around vertical axis.  $m_x$ ,  $m_y$  and  $J_z$  represent the added masses and added moment of inertia.  $x_G$  is the longitudinal center of gravity, where the midship is taken as origin of the coordinate system. Since the origin of ship-fixed coordinate system is defined on COG in CFD

simulations, the term  $Y_{HXG}$  is added to RHS of the yaw moment equation in Eqn.[1]. Dot notations of surge, sway and angular velocities refer to time derivative of the corresponding kinematical parameter. The moment of inertia is calculated approximately as  $I_z \cong m(0.25L_{pp})^2$ . In this study, the hydrodynamic forces and moment, the hydrostatic properties and the kinematical parameters are non-dimensionalized as given in Table 1.

**Table 1.** Non-dimensionalization of ship parameters.

Parameters	Non-dimensionalized by
$X, Y$	$0.5\rho U^2 LT$
$N$	$0.5\rho U^2 L^2 T$
$u, v$	$U$
$r$	$U/L$
$m, m_x, m_y$	$0.5\rho L^2 T$
$I_z, J_z$	$0.5\rho L^4 T$

### 2.3 Hull Forces and Moment

It has been assumed that the ship advance speed is sufficiently low and therefore the wave-making resistance is not dominant. Hydrodynamic forces and moment acting on the midship can then be described in terms of non-dimensional sway velocity ( $v'$ ) and yaw rate ( $r'$ ) as follows:

$$\begin{aligned}
 X'_H &= X'_0(u) + X'_{vv}v'^2 + (X'_{vr} + m' + m'_y)v'r' + (X'_{rr} + m'x'_G)r'^2 \\
 Y'_H &= Y'_v v' + (Y'_r - m' - m'_x)r' + Y'_{vvv}v'^3 + Y'_{vvr}v'^2 r' + Y'_{vrr}v'r'^2 + Y'_{rrr}r'^3 \\
 N'_H &= N'_v v' + (N'_r - m'x'_G)r' + N'_{vvv}v'^3 + N'_{vvr}v'^2 r' + N'_{vrr}v'r'^2 + N'_{rrr}r'^3
 \end{aligned} \tag{2}$$

where all coefficients ( $X'_{vv}$ ,  $Y'_{vvv}$ ,  $Y'_{vrr}$ ,  $N'_{rrr}$ , etc.) are defined as hydrodynamic derivatives or maneuvering coefficients for maneuvering motion, while  $X'_0(u)$  represents the total resistance coefficient in straight motion.  $X'_{vv}$ ,  $Y'_v$ ,  $Y'_{vvv}$ ,  $N'_v$ ,  $N'_{vvv}$  are obtained from static drift tests, ( $X'_{rr} + m'x'_G$ ), ( $Y'_r - m' - m'_x$ ),  $Y'_{rrr}$ , ( $N'_r - m'x'_G$ ),  $N'_{rrr}$  are determined by performing pure yaw test and ( $X'_{vr} + m' + m'_y$ ),  $Y'_{vvr}$ ,  $Y'_{vrr}$ ,  $N'_{vvr}$ ,  $N'_{vrr}$  can be obtained from combined yaw and drift test. It should be noted that predicted forces and moment ( $X'_H$ ,  $Y'_H$ ,  $N'_H$ ) in pure yaw and yaw and drift tests include added mass and centrifugal force terms.

### 2.4 Propeller Force

The hydrodynamic force due to propellers for a TPTR ship can be described as follows:

$$X_P^{P,S} = (1 - t_P^{P,S})\rho n_P^2 D_P^4 K_T^{P,S} \tag{3}$$

where the superscripts 'P' and 'S' mean port and starboard sides, respectively. Since the propellers are identical and rotating at the same revolutions per second (rps); the diameter ( $D_P$ ) and the propeller revolutions ( $n_P$ ) are taken equal for both propellers. Each of the propellers is rotating inward at constant rotation rate. In addition, it is assumed that the propellers' thrust deduction factors in straight ( $t_P^{P,S}$ ) and maneuvering motion ( $t_P^{P,S}$ ) are same for simplicity. The thrust coefficient ( $K_T^{P,S}$ ) which can be derived by quadratic polynomial fitting to open water characteristics can be given as the following:

$$K_T^{P,S} = k_0 + k_1 J_P^{P,S} + k_2 (J_P^{P,S})^2 \tag{4}$$

Here,  $k_0$ ,  $k_1$  and  $k_2$  are the coefficients of polynomial equation of advance ratio ( $J_P^{P,S}$ ).  $J_P^{P,S}$  is defined for TPTR ships as follows (Khanfir et al., 2011):

$$J_P^{P,S} = \frac{(1 - w_P^{P,S})(u + y_P^{P,S}r)}{n_P D_P} \quad [5]$$

where  $w_P$  is the wake coefficient during the maneuvering motion and  $y_P$  ( $y_P^S = -y_P^P$ ) is the offset of the propellers from the centerline. Since  $w_P$  changes during the maneuvering motion, it is usually estimated on the the wake coefficient in straight motion ( $w_{P0}^{P,S}$ ) as proposed by Inoue et al. (1981), which is given in Eqn. 6.

$$w_P^{P,S} = w_{P0}^{P,S} \exp(-4\beta_P^2) \quad [6]$$

The above-mentioned expression in Eqn.6 is originally given for SPSR ships; however, it is used for the present TPTR ship for simplicity as it was also adopted to a TPTR ship in another study (Liu et al., 2017).  $\beta_P$  is geometrical inflow angle to the propellers in maneuvering and can be derived as follow:

$$\beta_P = \beta - x_P' r' \quad [7]$$

where  $\beta$  is drift angle and  $x_P'$  is non-dimensional longitudinal distance of the propellers from midship ( $x_P/L$ ). Since both the propellers located at same longitudinal coordinate for the reference benchmark ship, the value of  $\beta_P$  can be assumed as equal for the propellers.

## 2.5 Rudder Forces and Moment

The forces and moment on the hull due to rudders can be expressed based on the rudder normal force ( $F_N^{P,S}$ ) as follows (Khanfir et al., 2011):

$$\begin{aligned} X_R &= -(1 - t_R)(F_N^P \sin \delta^P + F_N^S \sin \delta^S) \\ Y_R &= -(1 + a_H)(F_N^P \cos \delta^P + F_N^S \cos \delta^S) \end{aligned} \quad [8]$$

$$N_R = -(x_R + a_H x_H)(F_N^P \cos \delta^P + F_N^S \cos \delta^S) + (1 - t_R)(y_R^P F_N^P \sin \delta^P + y_R^S F_N^S \sin \delta^S)$$

where  $t_R$  is the steering resistance deduction factor and  $a_H$  is the rudder increase factor. Taking the midship as origin of the ship-fixed coordinate system,  $x_H$  is the non-dimensional longitudinal coordinate of acting point of the additional lateral force. These coefficients represent the interaction between hull and rudder. It is assumed that the rudders do not interact with each other as they are located sufficiently far away from the ship's centerline.  $x_R$  and  $y_R$  ( $y_R^S = -y_R^P$ ) denote the longitudinal and lateral coordinates of the rudders, respectively. The rudder normal force acting on rudders for a TPTR type ship is given by the following equation (Lee and Fujino, 2003):

$$F_N^{P,S} = 0.5 \rho A_R [(u_R^{P,S})^2 + (v_R^{P,S})^2] \frac{6.13 \Lambda}{\Lambda + 2.25} \sin \alpha_R^{P,S} \quad [9]$$

where  $\rho$  is the water density,  $A_R$  denotes the profile area of the moveable part of the rudder and  $A_R = A_R^P = A_R^S$ .  $\Lambda$  is the rudder aspect ratio and it is also taken same for both rudders. Furthermore, the effective inflow angle to the rudders ( $\alpha_R^{P,S}$ ) for ships with TPTR configuration is defined by the following equation (Khanfir et al., 2011):

$$\alpha_R^{P,S} = \delta^{P,S} - \delta_R^{P,S} \quad [10]$$

where  $\delta_R$  is the effective rudder angle at which the rudder normal force becomes zero. This angle is given as shown in the following equations.

$$\delta_R^{P,S} = \gamma_R^{P,S} \beta_R^{P,S} - \tan^{-1} \left( \frac{y_R^{P,S}}{x_p^{P,S}} \right) \quad [11]$$

$$\beta_R^{P,S} = \beta - l_R^{P,S} r' \quad [12]$$

Here,  $\gamma_R$  and  $l_R'$  ( $l_R/L$ ) are called flow straightening factors due to lateral speed and yaw rate of the ship, respectively. As reported in Kang et al. (2008),  $\gamma_R$  shows a variation during the port and starboard turnings, but  $l_R'$  is assumed to be constant in this study,  $l_R' \cong 2x_R$  (Kijima et al., 1990; Kim et al., 2007). The equations for the longitudinal ( $u_R$ ) and lateral ( $v_R$ ) inflow velocities to the rudder given in Eqn. 9, for TPTR ships are as follows:

$$u_R^{P,S} = \varepsilon^{P,S} u_p^{P,S} \sqrt{\eta \left\{ 1 + \kappa^{P,S} \left( \sqrt{1 + \frac{8K_T^{P,S}}{\pi(U_p^{P,S})^2}} - 1 \right) \right\}^2 + (1 - \eta)} \quad [13]$$

$$v_R^{P,S} = u_R^{P,S} \tan \delta_R^{P,S} \quad [14]$$

where  $u_p$  is the longitudinal inflow velocity to the propeller,  $u_p = (1 - w_p^{P,S})(u + y_p^{P,S}r)$ . Furthermore,  $\varepsilon$  indicates the ratio of wake fraction at rudder position ( $1 - w_R$ ) to that at propeller position ( $1 - w_p$ ).  $\kappa$  is a constant for expressing  $u_R$ , and  $\eta$  refers to ratio of the diameter of propeller to rudder span.

### 3. Computational Method

In order to calculate the hydrodynamic forces acting on the hull; the continuity and Navier-Stokes equations are discretized by a finite volume method (FVM) and solved numerically utilizing the commercial RANS solver STAR-CCM+. Incompressible flow condition is imposed on the viscous flow field and perturbations on the free surface are taken into account. The Volume of Fluid (VOF) method is adopted to capture the elevation of free surface. A SIMPLE algorithm is employed to solve pressure-velocity coupling. First-order backward Euler scheme is used for discretizing the temporal terms, while second-order upwind scheme is performed for the convection and diffusion terms. The  $k - \omega$  SST turbulence model with wall functions is applied to computational domain. This model performs the  $k - \varepsilon$  model in the far field region and adopted the  $k - \omega$  model for solving the near-wall flow (Menter, 1994).

In this study, Dynamic Fluid-Body Interaction (DFBI) option is activated to simulate the translation and rotation motions. In the DFBI approach, the rigid body executes the prescribed harmonic motion within the fluid domain. The DFBI module is used in the static drift and the dynamic PMM simulations for the ship which is free to heave and pitch motions; whereas the self-propulsion, the static rudder and the drift-rudder tests are simulated in a fixed-steady condition. Moving Reference Frame (MRF) technique is used to simulate the fluid flow around the rotating propellers. Time step size chosen for the static drift simulations is 0.04s, while it is determined as 0.01s for the dynamic PMM simulations. The following sections present the main particulars of ship model, the simulation matrix, the boundary conditions, the grid design and the methods for determination of hydrodynamic derivatives.

#### 3.1 Geometry and Simulation Conditions

The geometry selected for the present study is 1/46.588 scaled DTMB 5415 model (DTMB 5512), which is a TPTR ship appended with only bilge keels (<https://simman2014.dk>). This hull form, which is one of the benchmark models adopted by ITTC (International Towing Tank Conference), is used in

several studies for maneuvering predictions (Bhushan et al., 2011; Sakamoto et al., 2012a,b; Carrica et al., 2013; Yoon et al. 2015a,b; Woolliscroft and Maki, 2016, Duman et al., 2017, Duman and Bal, 2018). It should be noted that the propellers and rudders which are shown in Figure 2 are selected from those of MARIN 7967 model. The principal dimensions of the hull, propeller and rudder are listed in Table 2.

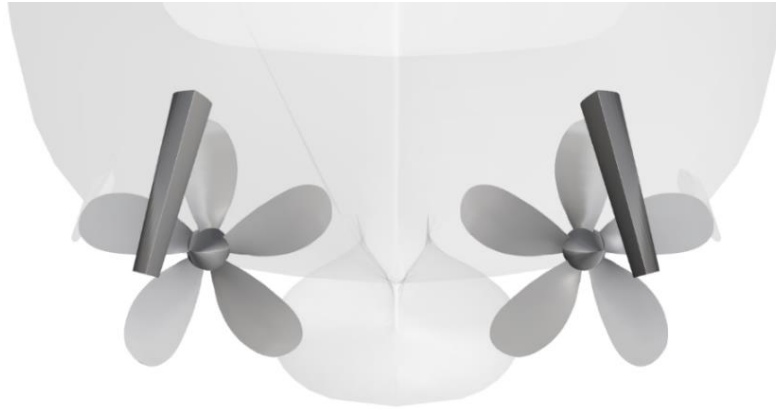


**Fig. 2.** Back view of the rudders and propellers of DTMB 5415.

**Table 2.** Main particulars of the DTMB 5512 model.

$\lambda = 1: 46.588$			
<i>Hull</i>		<i>Propellers</i>	
$L_{pp}(m)$	3.048	<i>Num. of Blades</i>	5
$L_{wl}(m)$	3.052	$D(m)$	0.132
$B_{wl}(m)$	0.409	$P/D (0.7R)$	0.870
$T(m)$	0.132	$A_E/A_0$	0.580
$C_B(-)$	0.506	<i>Rotation</i>	Inward
$C_M(-)$	0.821	<i>Hub Ratio</i>	0.160
$C_P(-)$	0.617	$x_P^{P,S}/L_{pp}$	-0.462
<i>Disp. Vol. (m<sup>3</sup>)</i>	0.083	$ y_P^{P,S} /B_{wl}$	0.244
$S(m^2)$	1.369	<i>Rudders</i>	
<i>LCB(%)</i> , fwd +	-0.683	$Span(m)$	0.094
$LCG(m)$	-0.016	$Lat. Area(m^2)$	0.007
$TCCG(m)$	0.000	<i>Aspect Ratio</i>	1.260
$VCCG(m)$	0.084	<i>Angle with vertical axis(deg)</i>	15
$L/B$	7.452	$x_R^{P,S}/L_{pp}$	-0.472
$B/T$	3.099	$ y_R^{P,S} /B_{wl}$	0.249
$U(m/s)$	1.531		

The simulation matrix for predicting hydrodynamic derivatives is built up with the test conditions of Yoon (2009) to validate the present CFD results. The static drift simulations are carried out for varying drift angles from  $0^\circ$  to  $20^\circ$ . Furthermore, two types of dynamic PMM simulations are performed. The pure yaw test is simulated for six maximum yaw rate up to  $r'_{max} = 0.75$ , while the yaw-drift simulation is performed for  $\beta = 9^\circ, 10^\circ, 11^\circ$  at a constant yaw rate,  $r'_{max} = 0.30$ . ITTC (7.5-02 06-02 rev. 5; 2017) recommends PMM motion frequencies to be in a given range so that the harmonic motions do not get affected by the physical structure of the tank or the dynamic motion of the ship. These frequencies are categorized under three different non-dimensional oscillation frequencies ( $\omega'_1 = \omega L/U$ ,  $\omega'_2 = \omega\sqrt{L/g}$ ,  $\omega'_3 = \omega U/g$ ). In the present numerical simulations, experimental test matrix of Yoon (2009) was followed and the frequencies adopted along with ITTC recommendations are shown in Table 3. The simulation matrix followed for estimating the propeller and the rudder parameters are given in Table 4. All simulations are carried out under the condition of  $Fr = 0.25$ . For the verification and validation study, the selected cases are static drift at  $\beta = 6^\circ$ , pure yaw at  $r'_{max} = 0.30$  and yaw-drift and drift at  $r'_{max} = 0.30$ ,  $\beta = 10^\circ$ .

**Table 3.** PMM motion frequencies and ITTC recommendations.

	Present PMM	ITTC Recommendations
$\omega'_1$	1.68~2.50	$2 < \omega'_1 < 4$
$\omega'_2$	0.40~0.71	$\omega'_2 \neq 1^*$
$\omega'_3$	0.13~0.19	$\omega'_3 \ll 0.25$

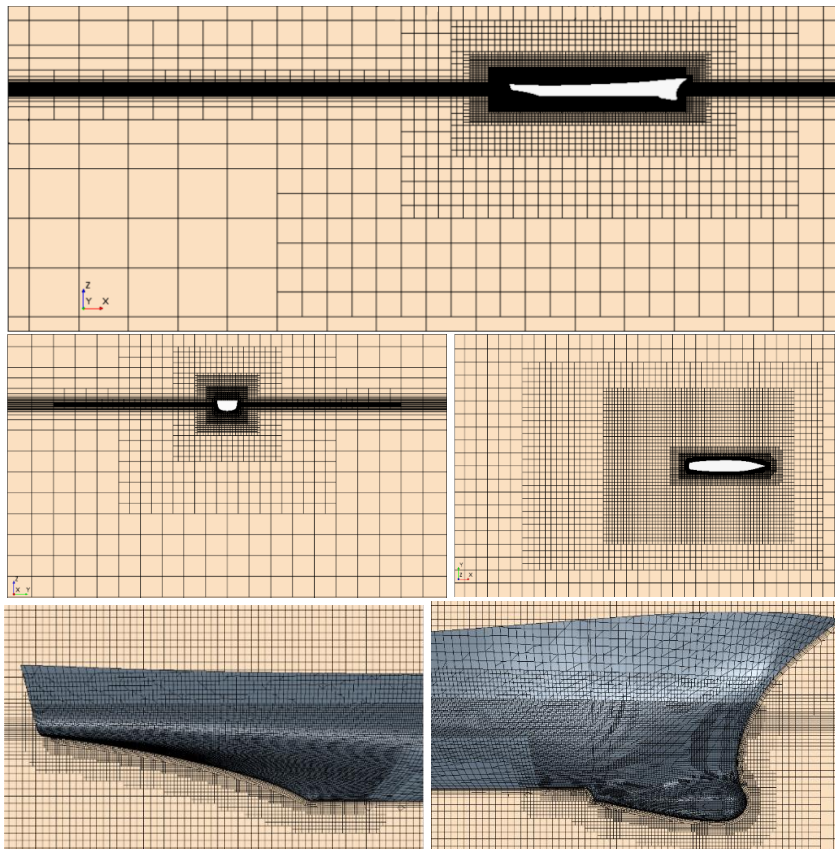
\*This value represents the tank resonance which occurs at  $\omega'_2 = \sqrt{\pi L/b}$ , where L is model length and b is tank width.

**Table 4.** Simulation matrix for the estimation of hull-propeller-rudder interaction parameters.

	$n_p(rps)$	$\delta(deg)$	$\beta(deg)$
Self-propulsion test	11.4	0	0
Static rudder test	10.6; 11.4; 12.2	0, 10, 20, 30, 35	0
Drift-rudder test	11.4	-20, -10, 0, 10, 20	0, 5, 10

### 3.2 Boundary Conditions and Grid Structure

A large rectangular-shaped domain is generated for the simulations, where the boundaries extend to  $1L_{pp}$  upstream from fore-perpendicular,  $3L_{pp}$  downstream from the aft-perpendicular. It has  $1.5L_{pp}$  distance to both sides from the centerline,  $0.5L_{pp}$  to top and  $1.5L_{pp}$  to bottom surfaces.

**Fig. 3.** Mesh structure in the computational domain and around the hull surface.

The origin of the ship-fixed coordinate system is located on the longitudinal center of gravity. The pressure outlet boundary condition is applied to the vertical border behind the vessel, while the inlet boundary condition is imposed for the rest of the boundaries, except that the symmetry boundary condition is used in the static drift simulations for the side walls. In addition, no-slip boundary condition is applied on the hull and rudder surfaces. A numerical wave damping is also applied to all boundaries except for the top and bottom surfaces to prevent the reflection of waves generated by ship motion. Moreover, a cylindrical domain is generated around the propellers, imposing an interface between the rectangular and cylindrical domains for the self-propulsion, static rudder and drift-rudder simulations.

The computational grid used for the simulations is rigid and unstructured, which dominantly consists of hexahedral elements. The local refinement volumes for the hull vicinity, bow, stern, bilge keels and rudders are generated to improve the accuracy of the flow resolution. The mesh structure also includes an anisotropic vertical refinement around the free surface in order to capture the interface between air and water properly. Furthermore, prism layers are used on the hull and rudder surfaces to simulate the near-wall flow accurately, with achieving a  $y^+$  value of approximately 40 along the hull. Briefly; 2.37M mesh elements for the static drift simulation, 2.72M for the dynamic PMM simulations and 1.37 M for the self-propulsion, the static rudder and the drift-rudder simulations are generated. The grid structure used in the simulations are shown in different views shown in Figure 3.

### 3.3 Calculation of Hydrodynamic Derivatives

The hydrodynamic derivatives can be evaluated from the time histories based on the motion equations of the MMG model given in Eqn.2. For the results computed from the static drift simulations at different drift angles ( $v$ ), Eqn.2 can be simplified as follows:

$$\begin{aligned} X_H &= -X_0 + X_{vv}v^2 \\ Y_H &= Y_vv + Y_{vvv}v^3 \\ N_H &= N_vv + N_{vvv}v^3 \end{aligned} \quad [15]$$

where a quadratic function  $y(v) = -a + bv^2$  can be fitted for the  $X_H$  values, while a cubic function  $y(v) = av + bv^3$  is needed to be curve-fitted to  $Y_H$  and  $N_H$  values to calculate the hydrodynamic derivatives. Thus,  $a = X_0, Y_v, N_v$  and  $b = X_{vv}, Y_{vvv}, N_{vvv}$  are first determined. On the other hand, a third-order Fourier Series (FS) can be fitted to each time histories of the forces and moment obtained from harmonic pure yaw ( $\psi = -\psi_{max}\cos\omega t; r = r_{max}\sin\omega t$ ) and yaw-drift simulations ( $\psi = -\psi_{max}\cos\omega t + \beta; r = r_{max}\sin\omega t; v = -U_C\sin\beta$ ) as given in the following equation.

$$f(t) = f_0 + \sum_{n=1}^3 f_{cn} \cos(n\omega t) + \sum_{n=1}^3 f_{sn} \sin(n\omega t) \quad [16]$$

Here  $\omega$  is the angular frequency of yaw motion ( $\omega = 2\pi f$ ),  $f(t)$  denotes the time histories of  $X_H, Y_H$  and  $N_H$ ,  $f_{cn}$  and  $f_{sn}$  are the  $n$ th-order *sine* and *cosine* FS coefficients, respectively. Using  $Y_H$  as an example based on Eqn.2, the simplified models and their harmonic forms are given in Eqns.17-18 for pure yaw and yaw-drift motions.

$$\begin{aligned} Y_H &= Y_r r + Y_{rrr} r^3 \\ Y_H &= Y_{S1} \sin\omega t + Y_{S3} \sin 3\omega t \end{aligned} \quad [17]$$

$$Y_H = Y_v v + Y_{vvv} v^3 + Y_r r + Y_{rrr} r^3 + Y_{vrr} v r^2 + Y_{vvr} v^2 r \quad [18]$$

$$Y_H = Y_0 + Y_{S1} \sin \omega t + Y_{C2} \cos 2 \omega t + Y_{S3} \sin 3 \omega t$$

Similar equations can be derived for  $X_H$  and  $N_H$  following the same methodology. The FS coefficients shown in Eqns.17-18 are calculated by using Fourier-integral equation as follows:

$$X_0, Y_0, N_0 = \frac{1}{T} \int_0^T f(t) dt$$

$$X_{Cn}, Y_{Cn}, N_{Cn} = \frac{2}{T} \int_0^T f(t) \cos(n\omega t) dt \quad [19]$$

$$X_{Sn}, Y_{Sn}, N_{Sn} = \frac{2}{T} \int_0^T f(t) \sin(n\omega t) dt$$

where  $T$  is the period of oscillating motion,  $T = 2\pi/\omega$ . After calculation of FS coefficients, the hydrodynamic derivatives can be evaluated by utilizing the ‘Single-Run (SR)’ or the low-order ‘Multiple-Run (MR<sub>L</sub>)’ methods (Yoon, 2009). For the SR method, there is no need to fit a function to the FS coefficients, so the derivatives can be calculated algebraically. However, MR<sub>L</sub> includes quadratic or cubic functions to be fitted with respect to kinematical parameters of interest such as  $v$ ,  $r_{max}$ . It should be noted that the subscript “L” for the latter method (MR<sub>L</sub>) means only the low-order (0<sup>th</sup> and 1<sup>st</sup>) harmonics are used to determine hydrodynamic derivatives. The expressions for the hydrodynamic derivatives to be obtained with SR and MR<sub>L</sub> methods are shown in Table 5 and Table 6, respectively.

**Table 5.** Determination of the hydrodynamic derivatives by SR method.

Pure Yaw	Yaw-Drift
$X'_{rr} = -\frac{2}{r'_{max}} X'_{C2}$	$X'_{vr} = \frac{1}{v' r'_{max}} X_{S1}$
$Y'_r = \frac{1}{r'_{max}} (Y'_{S1} + 3Y'_{S3})$	$Y'_{vvr} = (Y'_{S1} - Y'_r r'_{max} - \frac{3}{4} Y'_{rrr} r'^3_{max}) / v'^2 r'_{max}$
$N'_r = \frac{1}{r'_{max}} (N'_{S1} + 3N'_{S3})$	$N'_{vvr} = (N'_{S1} - N'_r r'_{max} - \frac{3}{4} N'_{rrr} r'^3_{max}) / v'^2 r'_{max}$
$Y'_{rrr} = -\frac{4}{r'^3_{max}} Y'_{S3}$	$Y'_{vrr} = 2(Y'_0 - Y'_v v' - Y'_{vvv} v'^3) / v' r'^2_{max}$
$N'_{rrr} = -\frac{4}{r'^3_{max}} N'_{S3}$	$N'_{vrr} = 2(N'_0 - N'_v v' - N'_{vvv} v'^3) / v' r'^2_{max}$

**Table 6.** Determination of the hydrodynamic derivatives by MR<sub>L</sub> method.

Dynamic PMM Tests	Dependent Variable	Independent Variable	Fitted Function	Hydrodynamic Derivatives
Pure Yaw	$X'_0$	$r'_{max}$	$A + Bx^2$	$X'_* = A; X'_{rr} = 2B$
	$Y'_{S1}, N'_{S1}$	$r'_{max}$	$Ax + Bx^3$	$Y'_r, N'_r = A;$ $Y'_{rrr}, N'_{rrr} = 4B/3$
Yaw-Drift	$X'_{S1}$	$v'$	$Ax$	$X'_{vr} = A/r'_{max}$
	$Y'_0, N'_0$	$v'$	$Ax + Bx^3$	$Y'_{vrr} = 2(A - Y'_v) / r'^2_{max};$ $N'_{vrr} = 2(A - N'_v) / r'^2_{max}$
	$Y'_{S1}, N'_{S1}$	$v'$	$A + Bx^2$	$Y'_{vvr}, N'_{vvr} = B/r'_{max}$

#### 4. Verification and Validation

A verification and validation (V&V) study is performed for the grid spacing to estimate the numerical uncertainty in the CFD simulations. In this study, a widely-used methodology proposed by Stern et al. (2001) for CFD simulation results is followed. The results of pure yaw at  $r'_{max} = 0.30$ , combined yaw and drift at  $r'_{max} = 0.30$ ,  $\beta = 10^\circ$  and the static drift at  $\beta = 6^\circ$  are concerned. The V&V study focuses on  $X'$ ,  $Y'$  and  $N'$  for the static drift test, while the convergence of FS coefficients ( $X'_0, Y'_0, N'_0, X'_{S1}, Y'_{S1}, N'_{S1}$ ) is considered for the pure yaw and yaw-drift cases. Therefore, three different grid spacings are determined to evaluate the numerical uncertainty within the computed results. As it is hard to estimate the grid uncertainty ( $U_G$ ) in unstructured meshes,  $U_G$  is estimated based on the Richardson extrapolation method (Simonsen et al., 2012). The results are obtained for the grid convergence with three mesh numbers based on the refinement ratio of  $\sqrt{2} \cong 1.414$ . This leads to the mesh sizes ranging from 1.2M to 5.4M for the static drift test, while it has a range of 1.4M to 5.8M for the dynamic PMM cases. As stated before, the time step size is selected as 0.04s for the static drift simulations and 0.01s for the pure yaw and yaw-drift simulations. All results of non-dimensionalized forces, moment and FS coefficients for different grid spacings are given in Table 7.

**Table 7.** Non-dimensional coefficients computed with different number of grid elements for the static drift, pure yaw and yaw-drift simulations, Fr=0.280.

Test Type	Quantities	Number of Elements			EFD
Static Drift, $\beta = 6^\circ$		1.17M ( $S_3$ )	2.38M ( $S_2$ )	5.38M ( $S_1$ )	Data (D)
	$X'$	-0.01889	-0.01830	-0.01794	-0.01870
	$Y'$	0.03662	0.03580	0.03522	0.03350
	$N'$	0.01675	0.01689	0.01681	0.01802
Pure Yaw, $r'_{max}=0.30$		1.39M	2.73M	5.78M	Data
	$X'_0$	-0.01790	-0.01764	-0.01773	-0.01890
	$Y'_{S1}$	-0.01706	-0.01770	-0.01794	-0.01595
	$N'_{S1}$	-0.01437	-0.01442	-0.01438	-0.01461
Yaw-Drift, $r'_{max}=0.30$ $\beta = 10^\circ$		1.39M	2.73M	5.78M	Data
	$X'_{S1}$	0.00065	-0.00069	-0.00124	-0.00463
	$Y'_0$	0.06283	0.06591	0.06496	0.07102
	$N'_0$	0.03085	0.03240	0.03242	0.03333
	$Y'_{S1}$	-0.02712	-0.02909	-0.02919	-0.02928
	$N'_{S1}$	-0.02075	-0.02172	-0.02146	-0.02151

For the verification process, once the quantities are computed, the difference between the results of coarse-medium ( $S_3 - S_2$ ) and medium-fine ( $S_2 - S_1$ ) meshes, and the convergence ratio ( $R_{G,T}$ ) is calculated as follows:

$$\begin{aligned}\varepsilon_{G_{32}} &= S_3 - S_2 \\ \varepsilon_{G_{21}} &= S_2 - S_1 \\ R_G &= \varepsilon_{G_{21}} / \varepsilon_{G_{32}}\end{aligned}\quad [20]$$

where the subscript 'G' refers to grid. Based on the value of  $R_G$ , four different conditions may occur: i) monotonic convergence (MC) for  $0 < R_G < 1$ ; ii) oscillatory convergence (OC) for  $-1 < R_G < 0$ ; iii)

monotonic divergence (MD) for  $R_G > 1$  and iv) oscillatory divergence (OD) for  $R_G < -1$ . A generalized Richardson extrapolation (RE) technique is used for MC to estimate the uncertainties ( $U_G$ ) and errors ( $\delta_{RE_G}^*$ ), whereas only  $U_G$  is calculated for the OC condition as given in the following way:

$$U_G = \left| \frac{1}{2}(S_U - S_L) \right| \quad [21]$$

where  $S_U$  and  $S_L$  mean the upper and lower limits of oscillating solution, respectively. The numerical uncertainty and error can not be estimated for MD and OD conditions as the solutions diverge. For the condition of MC, the numerical error  $\delta_{RE_{G1}}^*$  and the order of accuracy  $p_G$  are estimated using the RE as follows:

$$\delta_{RE_{G1}}^* = \frac{\varepsilon_{G21}}{r_G^{p_G} - 1} \quad [22]$$

$$p_{Gest} = \frac{\ln(\varepsilon_{G32}/\varepsilon_{G21})}{\ln(r_G)} \quad [23]$$

where  $r_G$  is the refinement ratio which is considered as  $\sqrt{2}$  for the variation of grid spacing. Furthermore, a correction factor ( $C_G$ ) is defined to correct Eqn.22 for the effects of higher order terms in the expression of RE, which is calculated as:

$$C_G = \frac{r_G^{p_G} - 1}{r_G^{p_{Gest}} - 1} \quad [24]$$

where  $p_G$  is the theoretical order of accuracy for the numerical method, which is 2 in this study. If  $C_G$  is close to 1, which shows how close the solutions are to the asymptotic range, then the numerical error  $\delta_{SN}^*$ , the benchmark result  $S_C$  and the corrected grid uncertainty  $U_{GC}$  can be calculated as follows (Simonsen et al., 2012).

$$\delta_{SN}^* = C_G \delta_{RE_{G1}}^* \quad [25]$$

$$S_C = S - \delta_{SN}^* \quad [26]$$

$$U_{GC} = \begin{cases} (2.4(1 - C_G)^2 + 0.1) |\delta_{RE_{G1}}^*|, & |1 - C_G| < 0.125 \\ |1 - C_G| |\delta_{RE_{G1}}^*|, & |1 - C_G| \geq 0.125 \end{cases} \quad [27]$$

If the correction factor  $C_G$  is sufficiently less or greater than 1, which indicates the solutions are not close to asymptotic range, the numerical error is calculated as given in Eqn.22 and the numerical uncertainty  $U_G$  is estimated as given in Eqn.28.

$$U_G = \begin{cases} (9.6(1 - C_G)^2 + 1.1) |\delta_{RE_{G1}}^*|, & |1 - C_G| < 0.125 \\ (2|1 - C_G| + 1) |\delta_{RE_{G1}}^*|, & |1 - C_G| \geq 0.125 \end{cases} \quad [28]$$

For the validation process, the absolute error  $|E|$  between the EFD data and the CFD results is compared to the validation uncertainty  $U_V$ , which is calculated as:

$$U_V = \sqrt{U_G^2 + U_D^2} \quad [29]$$

where  $U_D$  is the total experimental uncertainty. In order to calculate validation uncertainty ( $U_V$ ),  $U_D$  is taken from the experimental data of Yoon (2009). If the value of  $|E|$  is found to be smaller than that

of  $U_V$ , it means that the validation is achieved at the  $U_V$  level. The results of verification and validation studies for the static drift, pure yaw and yaw-drift are shown separately in Table 8, Table 9 and Table 10, respectively.

**Table 8.** V&V results for the static drift case at  $\beta = 6^\circ$ ,  $Fr = 0.280$ .

	$X'$	$Y'$	$N'$
<i>Condition</i>	MC	MC	OC
$\varepsilon_{G_{21}}$	0.00036	-0.00057	-0.00008
$\varepsilon_{G_{32}}$	0.00059	-0.00083	0.00014
$R_G$	0.61	0.69	-0.57
$p_{Gest}$	1.43	1.01	-
$C_G$	0.64	0.41	-
$U_G \% S_1$	5.41	8.64	0.42
$U_{G_C} \% S_1$	1.16	2.37	-
$ E  \% D$	4.06	5.13	6.71
$U_V \% D$	5.52	9.71	2.82

**Table 9.** V&V results for the pure yaw case at  $r'_{max} = 0.30$ ,  $Fr = 0.280$ .

	$X'_0$	$Y'_{S1}$	$N'_{S1}$
<i>Condition</i>	OC	MC	OC
$\varepsilon_{G_{21}}$	-0.00009	-0.00064	-0.00006
$\varepsilon_{G_{32}}$	0.00026	-0.00024	0.00004
$R_G$	-0.35	0.38	-0.80
$p_{Gest}$	-	2.83	-
$C_G$	-	1.67	-
$U_G \% S_1$	0.73	1.87	0.17
$U_{G_C} \% S_1$	-	0.53	-
$ E  \% D$	6.19	12.83	1.57
$U_V \% D$	7.63	2.12	1.21

**Table 10.** V&V results for the yaw-drift case at  $r'_{max} = 0.30$ ,  $\beta = 10^\circ$ ,  $Fr = 0.280$ .

	$X'_{S1}$	$Y'_0$	$N'_0$	$Y'_{S1}$	$N'_{S1}$
<i>Condition</i>	MC	OC	MC	MC	OC
$\varepsilon_{G_{21}}$	-0.00055	-0.00094	0.00001	-0.00009	0.00026
$\varepsilon_{G_{32}}$	-0.00134	0.00308	0.00155	-0.00197	-0.00097
$R_G$	0.41	-0.31	0.02	0.05	-0.27
$p_{Gest}$	2.57	-	12.55	8.92	-
$C_G$	1.44	-	76.54	21.01	-
$U_G \% S_1$	57.98	2.37	0.12	0.62	2.26
$U_{G_C} \% S_1$	9.35	-	0.06	0.29	-
$ E  \% D$	73.22	8.53	2.73	0.31	0.23
$U_V \% D$	16.88	4.28	2.01	3.75	3.01

As shown in Tables 8-10, all quantities considered here converge as the computational mesh is refined. It should be noted that  $U_{SN} = U_G$  is assumed for this study since the iteration uncertainty  $U_I$  is calculated smaller approximately two orders of magnitude than the corresponding  $U_G$  value. Therefore  $U_I$  values are ignored for all three grids. For the static drift test, surge ( $X'$ ) and sway ( $Y'$ ) forces show a monotonic convergence, while an oscillatory convergence is observed for yaw moment ( $N'$ ). For the static drift case, grid uncertainties  $U_G \% S_1$  are estimated for all the quantities within 9%. If the correction factor  $C_G$  is used which is close to 1 for  $X'$ , the value of  $U_G$  can be considered as  $U_{G_C} = 1.16\%$ . Concerning the grid uncertainties in pure yaw results,  $X'_0$  and  $N'_{S1}$  converged oscillatory while  $Y'_{S1}$  has a monotonic type condition. Comparing  $U_G \% S_1$  values with those of static drift case, it is found very small for FS coefficients within 2%. It is not needed to use  $C_G$  as the level of  $U_G \% S_1$  values is sufficiently small. On the other hand, five FS coefficients are considered for grid convergence study for

the combined yaw and drift case. Similar to the grid uncertainty results of pure yaw case,  $U_G \% S_1$  values are estimated around 1-2% except for the  $X'_{S1}$  results. This is most likely due to the existence of phase shifts in time histories of surge force. However, if  $C_G$  value is assumed to be close to 1, then the grid uncertainty can be corrected as  $U_{Gc} = 9.35\%$ .

The validation process is done using the comparison of relative error between the simulation result and experimental data, and validation uncertainty  $U_V$  as shown in Tables 8-10. If the error  $|E|$  is smaller than  $U_V$ , it means that the simulation results are not validated. As given in Eqn. 9, the experimental uncertainty  $U_D$  should be included if it exists to calculate  $U_V$ . The validation of error  $|E|$  is achieved for  $X'$  and  $Y'$  at the level of  $U_V = 5.52\%D$  and  $9.71\%D$  in the static drift simulation while it is achieved at  $7.63\%D$  for only  $X'_0$  in pure yaw. For the yaw-drift case, the validation of comparison error  $|E|$  for  $Y'_{S1}$  and  $N'_{S1}$  is obtained at the level of  $U_V = 3.75\%D$  and  $3.01\%D$ , respectively.

## 5. Numerical Results

Hydrodynamic forces and moment acting on the hull, propeller and rudder are numerically obtained from CFD simulations and presented in this section. Results obtained from static drift, dynamic PMM, self-propulsion and rudder simulations are used to calculate the relevant hydrodynamic derivatives. These derivatives are then used to draw the trajectory of the ship at specified conditions in turning circle and zigzag maneuvering tests.

### 5.1 Hull Forces and Moment

Hydrodynamic forces and moment acting on the ship is first computed by performing static drift, pure yaw and combined yaw-drift tests to evaluate the hydrodynamic derivatives in the MMG model. The predicted force and moment results are validated with those of experimental data from Yoon, 2009.

#### 5.1.1 Static Drift

Static drift simulations are relatively easier to handle as compared to the PMM tests. However, resolution of free water surface still has problems that could alter the forces and moment acting on the ship (Kinaci et al., 2016). Therefore, the wave cut values computed numerically has been validated with the experimental data given in Yoon et al. (2014). The comparison is given in Figure 4. It can be noted that the computed wave elevation at the given location is in satisfactory agreement with EFD data, except for bow region.

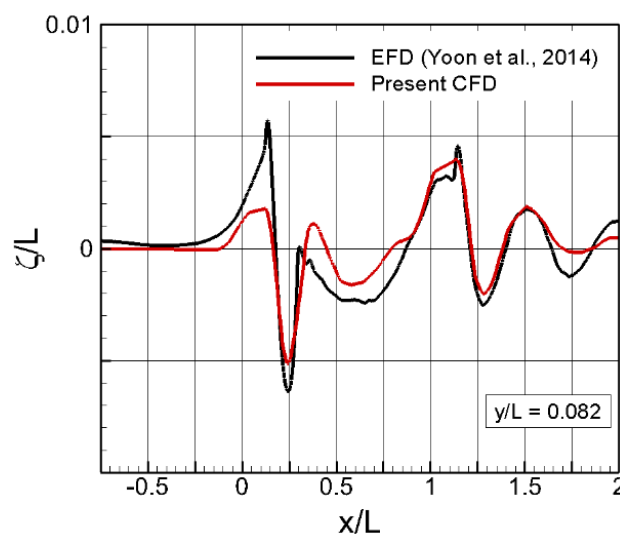


**Fig. 4.** Comparison of free surface elevations at  $y/L=0.082$ ,  $\beta=0^\circ$ ,  $Fr=0.280$ .

The dimensionless forces and moment obtained at different drift angles ( $\beta$ ) for static condition are compared with measured data as shown in Figure 5. Hull drift angle was changed from  $0^\circ$  to  $20^\circ$  as in the experiments. The variation in drift angle causes an increase in the sway force and yawing moment during the static drift simulations where the asymmetric flow occurs around the hull. It can be noted that the computed forces are in good agreement with EFD data, however there is a slight discrepancy between the results of EFD and CFD as the drift angle is becoming larger. The average relative errors ( $\bar{E}\%D$ ) of  $X'$ ,  $Y'$  and  $N'$  at  $Fr = 0.280$  are found as 3.9%, 8.9% and 7.8%, respectively. The reason for underestimation of  $Y'$  and  $N'$  at higher drift angles might be due to inaccurate prediction of flow separations and vortical flow structures around the hull. Experimental and numerical flow investigations for these inaccurate predictions at higher drift angles have become a popular research topic in recent years (Bhushan et al., 2011; Xing et al., 2012; Falchi et al., 2014).

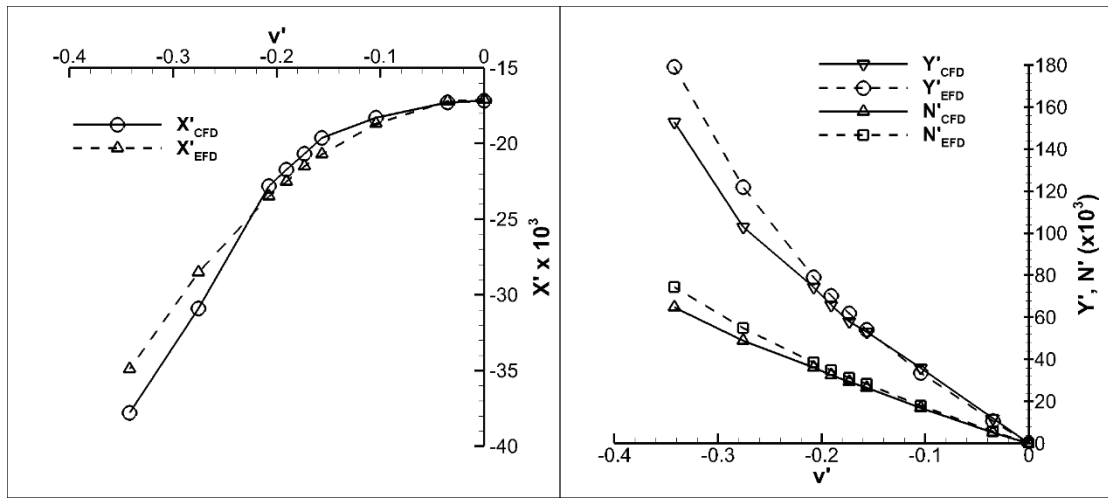


**Fig. 5.** Comparison of predicted hydrodynamic forces and yawing moment results with measured data (Yoon, 2009) for different drift angles ( $v' = -\sin\beta$ ).

### 5.1.2 Pure Sway and Yaw

In dynamic PMM simulations such as pure sway, pure yaw or combined yaw-drift, all forces and moments are to be analyzed from the third or subsequent cycles to avoid transverse effects at the beginning of the simulation (Shenoi et al., 2014). However in this study, it has been observed that the time histories of the second and third periods are almost same. Hence the results reported here for dynamic PMM simulations are from the second period of PMM to keep the computational time as short as possible.

The pure sway simulations were performed at three different maximum sway velocities ( $v'_{max}$ ) at  $Fr = 0.280$ . In the pure sway simulations, the primary focus is to estimate the sway-acceleration derivative ( $Y'_v$ ). First, the local flow field around the hull at different locations ( $x/L = 0.135; 0.235; 0.735; 0.935$ ) and phases ( $\gamma = 0^\circ; 90^\circ$ ) in pure sway simulation was estimated by CFD and compared with measured PIV results (Yoon, 2009) in terms of dimensionless axial velocity ( $U$ ). Figure 6 shows the contours where the sway velocity ( $v'$ ) reaches its maximum (at  $\gamma = 0^\circ$ ) and minimum (at  $\gamma = 90^\circ$ ) values. The predicted contours generally show good agreement with PIV data at both phase angles; the major difference between the two contours is in vortex cores. This flaw might be handled by increasing the grid resolution around the hull. The sway added mass ( $m'_y$ ) and moment of inertia ( $J'_z$ ) terms are obtained by pure sway and pure yaw simulations, and an empirical formula proposed by Zhou et al. (1983) based on the charts given by Motora (1958) and Motora (1960a,b). In this study,  $m'_x$  is taken as 5% of ship mass ( $m' = 0.1394$ ) as suggested by Clarke et al. (1983), while  $m'_y$  and  $J'_z$  which equal to  $-Y'_v$  and  $-N'_r$  respectively, were determined by performing pure sway and yaw

simulations as given in Table 11. It can be said that the present CFD results show a reasonable agreement with the empirical result and EFD data.

**Table 11.** Comparison of added mass and moment of inertia obtained with different methods.

	<i>Present CFD</i>	<i>Empirical (Zhou et al.,1983)</i>	<i>EFD (Yoon,2009)</i>
$m'_y$	0.1082	0.1257	0.1135
$J'_z$	0.0078	0.0098	0.0070

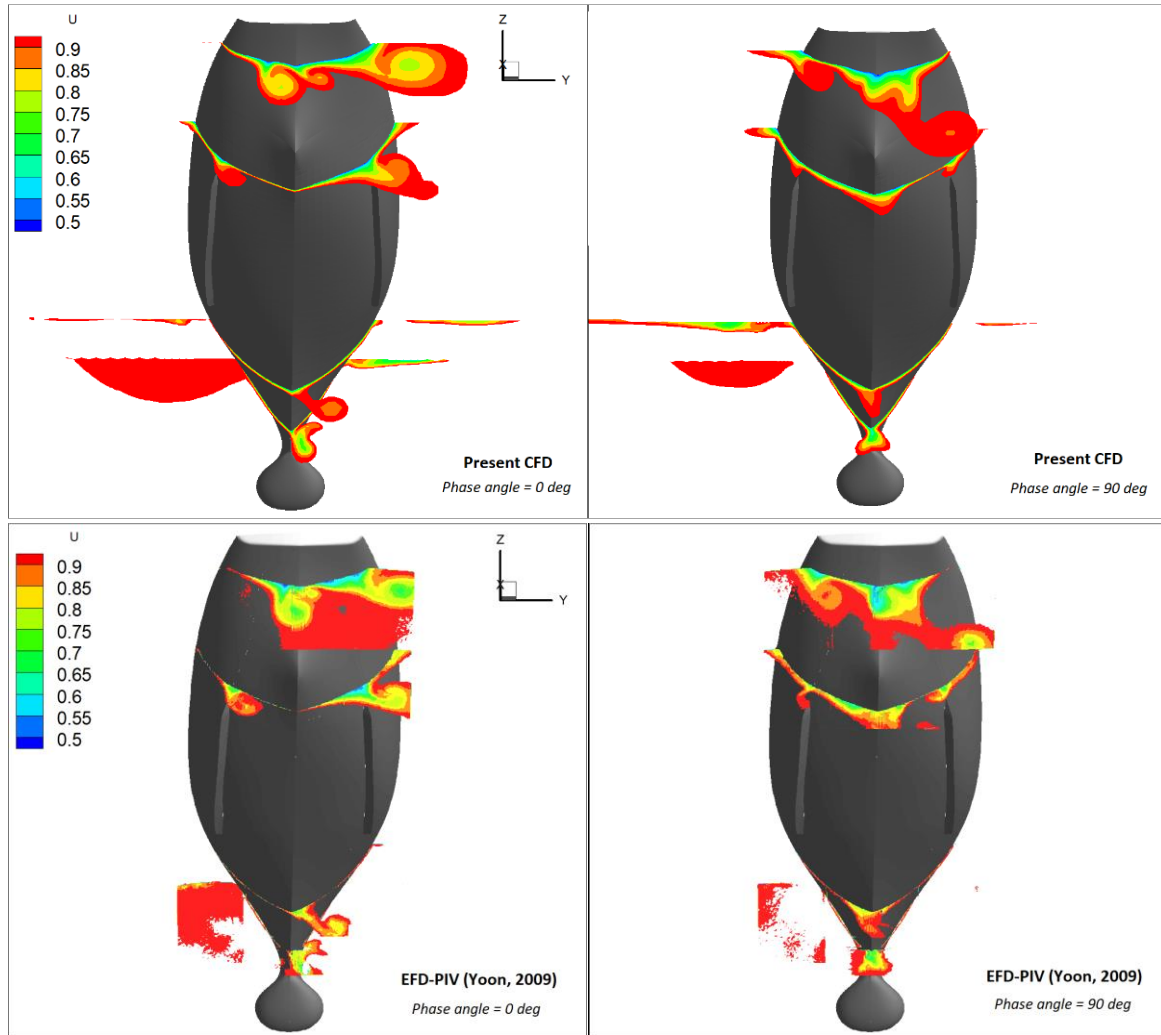


**Fig. 6.** Comparison of axial velocities at different motion phases in pure sway for  $Fr=0.280$ .

In pure yaw simulation, the main purpose is to estimate the hydrodynamic derivatives such as  $X'_{rr}, Y'_r, Y'_{rrr}, N'_r, N'_\dot{r}, N'_{rrr}$ . Therefore, the time histories of the forces and moment over one PMM period are predicted by CFD simulations and the results are compared with EFD data in Figure 7 for six different  $r'_{max}$  values. The overall trend indicates that the numerical results are compatible with EFD data for the sway force and yawing moment. It is also noted that the peak values for the sway force and yawing moment increase with an increment in  $r'_{max}$ .

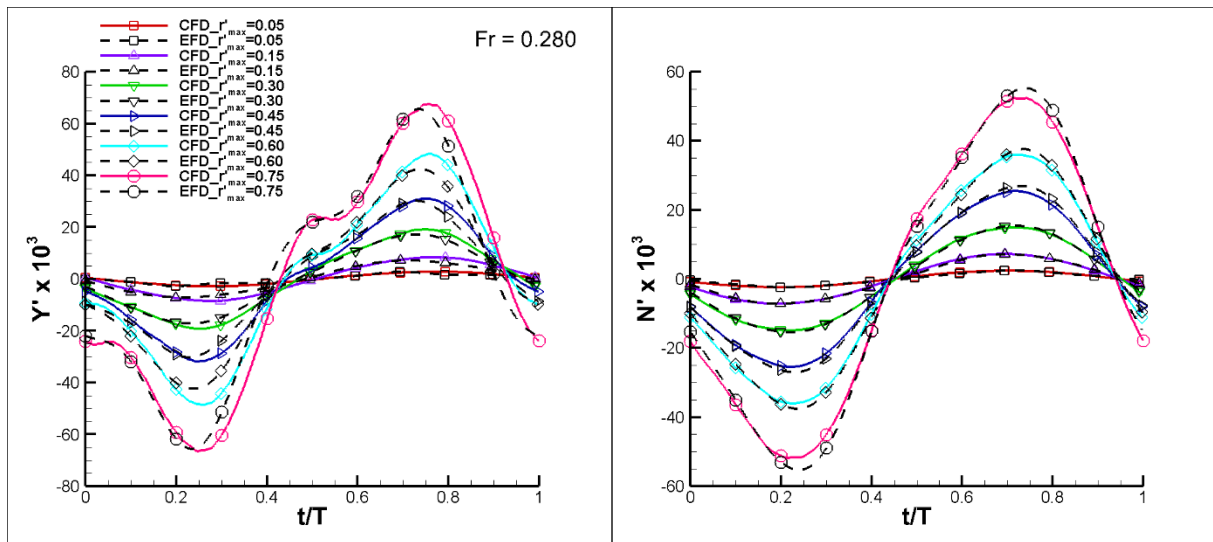


**Fig. 7.** Comparison of predicted values with EFD data (Yoon, 2009) in pure yaw motion for different  $r'_{max}$  values.

The average values of  $X'$  are given in Figure 8 since showing all time histories of surge force for different  $r'_{max}$  values in a single figure may lead to a confusion. Although there are some slight phase shifts in the surge force, the average values of time histories agree well with the EFD within an average deviation of 6.7% ( $\bar{E}\%D$ ). It was stated by (Woolliscroft and Maki, 2016) that the phase shifts in surge force may occur due to turbulence modelling, wall functions or boundary conditions. From Figure 8, although it is seen that CFD underestimates the surge force, a similar trend can be observed for both methods as  $r'_{max}$  increases.

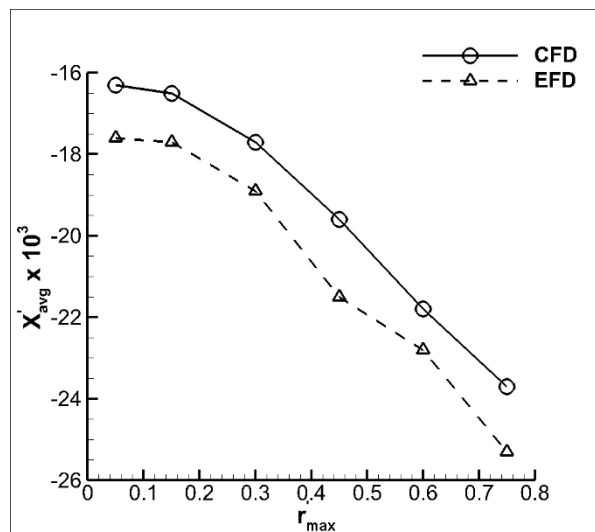


**Fig. 8.** Comparison of average surge forces in pure yaw motion for different  $r'_{max}$  values.

### 5.1.3 Combined Yaw and Drift

In the combined yaw-drift test, the model still performs a yaw motion but has a fixed drift angle at the same time. The purpose here is to estimate the cross-coupled derivatives such as,  $X'_{vr}$ ,  $Y'_{vvr}$ ,  $Y'_{vrr}$ ,  $N'_{vvr}$ ,  $N'_{vrr}$ . Comparison of  $Y'$  and  $N'$  values for different yaw-drift simulations are plotted in Figure 9. Unlike the pure yaw test, asymmetric side force and yawing moment results are observed during the motion because of the effect of drift angle. It seems that the trend of the curves is similar to each other and the experimental data satisfactorily captured by CFD. Moreover, the

amplitude of side force and yawing moment increase as the drift angle increases. Note that the non-dimensional maximum yaw rate ( $r'_{max}$ ) is kept fixed at  $r'_{max} = 0.3$  for all yaw-drift simulations.

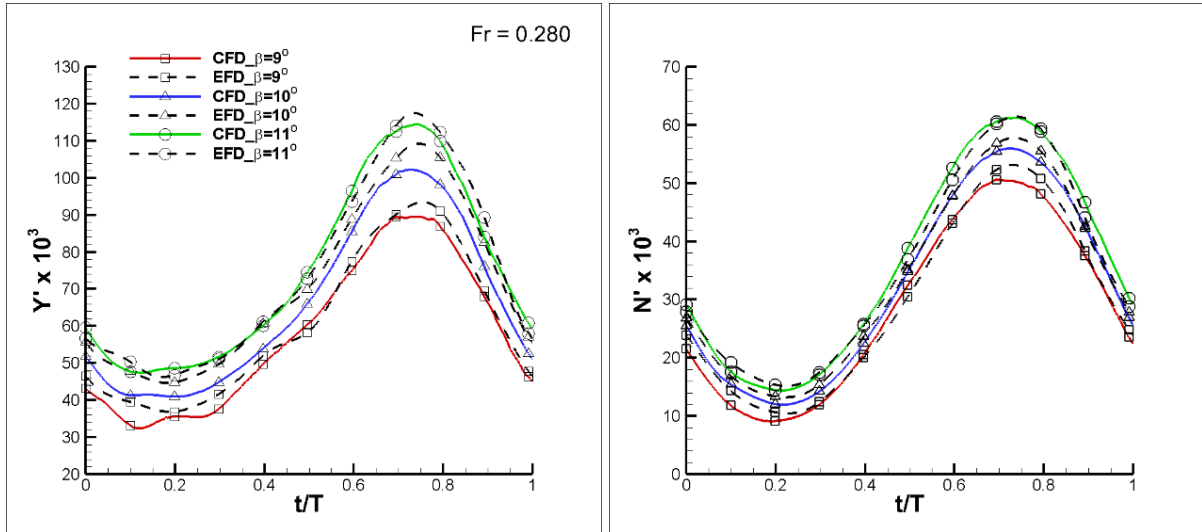


**Fig. 9.** Comparison of predicted sway force and yawing moment with EFD data (Yoon, 2009) in yaw-drift simulation.

For surge force, neither the general trend of the curves nor their peaks are match. The mismatch may partly be attributed to the experimental noise. Relative differences ( $E\%D$ ) of the average surge force results are calculated as 3.2%, 3.9% and 6.3% for 9, 10, 11 degrees of drift angles, respectively.

## 5.2 Propeller Force

The reference ship is fitted with two inward-rotating propellers, which both have the same distance to the centerline of the ship. Therefore, lateral side forces due to propellers can be assumed to cancel out each other ( $Y_p^{P,S} = 0$ ). The only hydrodynamic force generated by the propellers is the surge force ( $X_p^{P,S}$ ). The self-propulsion test is performed by taking the free surface effect into consideration to predict the thrust, propeller revolution and hull-propeller interaction factors.

Open water characteristics of the propellers ( $k_0, k_1, k_2$ ) in the calculation of  $K_T$  are taken from the experimental data of MARIN (<https://simman2014.dk>). The propeller revolutions under the self-propulsion point of the model are estimated by CFD for  $Fr = 0.25$ .  $t_p$  is determined by considering the resistance results of bare hull and self-propulsion simulations, while  $w_{p0}$  is found from the open water characteristics by applying the thrust identity method (ITTC, 7.5-02 03-01.4). It is assumed that all parameters obtained for port side propeller are same as the starboard side since they have identical geometry. The results predicted for the propeller force at full scale are summarized in Table 12.

**Table 12.** Predicted parameters for propeller force at full scale for  $Fr = 0.25$ .

Parameters	Source	Value
$k_0^{P,S}$	MARIN test data	0.3984
$k_1^{P,S}$	MARIN test data	-0.2997
$k_2^{P,S}$	MARIN test data	-0.1405
$n_p^{P,S}$ (rps)	Self-propulsion simulation	1.65
$t_p^{P,S}$	Resistance and self-propulsion simulation	0.21
$w_{p0}^{P,S}$	Thrust identity method	0.0726

### 5.3 Rudder Forces and Moment

The hull-rudder interaction parameters such as  $t_R$ ,  $a_H$ ,  $x'_H$  are calculated by performing static rudder simulations ( $\beta = 0^\circ$ ) at constant propeller revolution ( $n_p^{P,S} = 11.4 \text{ rps}$ ). In the simulations, the rudder angles vary from  $0^\circ$  to  $35^\circ$ . The interaction coefficients found are assumed to be equal for both rudders. Figure 10 shows the change of hydrodynamic forces and moment with respect to the longitudinal and lateral components of rudder normal force.

For a twin rudder system, Kang et al. (2008) shows that  $t_R$  does not change with the propeller load, whereas a slight variation is observed for  $a_H$  and  $x'_H$ . In this study, this variation is neglected and all interaction coefficients are determined under  $n_p^{P,S} = 11.4 \text{ rps}$  which is the representative propeller revolution of the reference ship. According to Eqn.8, the hull-rudder interaction coefficients can be determined utilizing the slopes of the fitting curves shown in Figure 10. The slope of the  $X - F_N \sin \delta$  curve gives  $(1 - t_R)$ , while  $a_H$  is calculated from the slope of  $Y - F_N \cos \delta$ .  $t_R$  here denotes the deduction in the resistance of rudders and  $a_H$  represents the increment in the lateral force acting on the hull due to steering (Yasukawa and Yoshimura, 2015). Longitudinal acting position of  $a_H$  is defined as  $x'_H$  and it is generally given in nondimensional form. Using the known values of  $a_H$  and the longitudinal position of the rudders at the stern part of the ship,  $x'_R = -0.4718$ ,  $x'_H$  can be obtained easily by the slope of  $N - F_N \cos \delta$  curve which gives  $(x'_R + a_H x'_H)$ . From the numerical results depicted in Figure 10, the hull-rudder interaction coefficients are calculated as  $t_R = 0.4404$ ,  $a_H = 0.0858$  and  $x'_H = -0.4357$ , where the minus sign means that the action point of  $a_H$  is located at the aft side of the ship. In Figure 10,  $F_N$  represents the total rudder normal force which is the summation of  $F_N^P$  and  $F_N^S$ ;  $F_N = F_N^P + F_N^S$ . Also the independent (y) and dependent (x) variables of equations given in the following figures show the corresponding values on y and x axis, respectively.

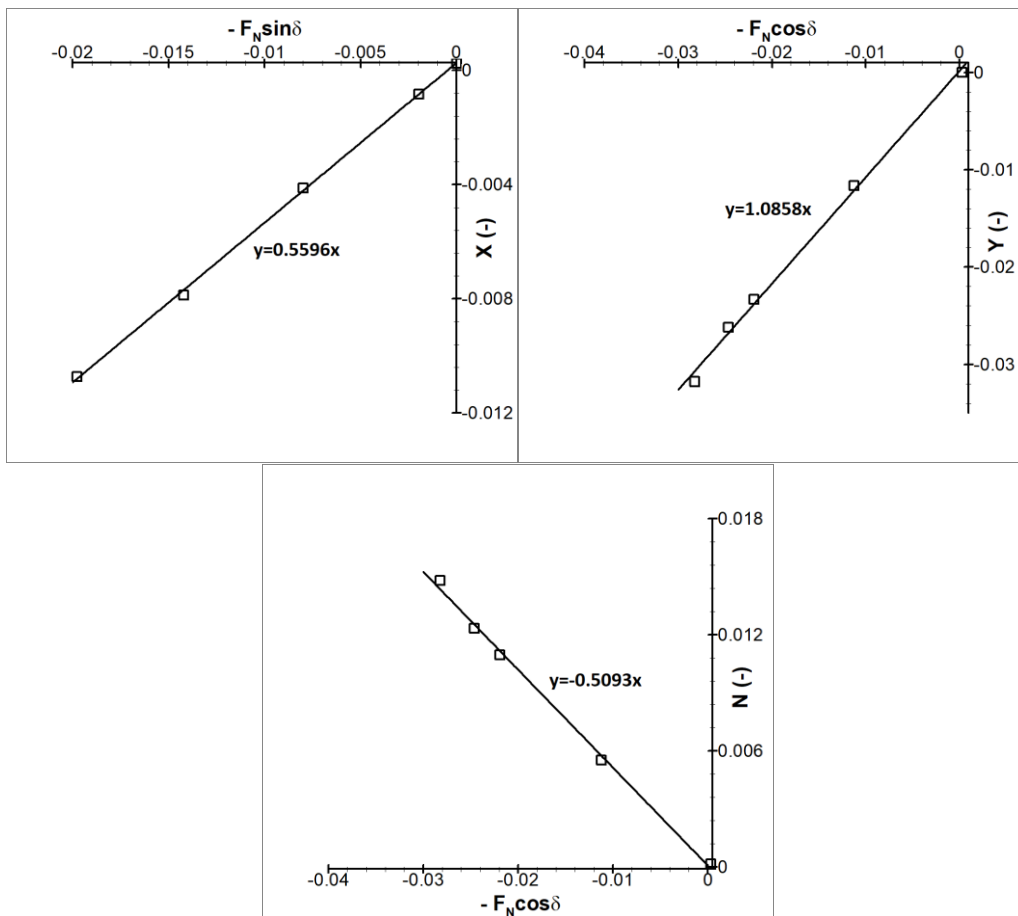


Fig. 10. Static rudder simulations for hull-rudder interaction parameters.

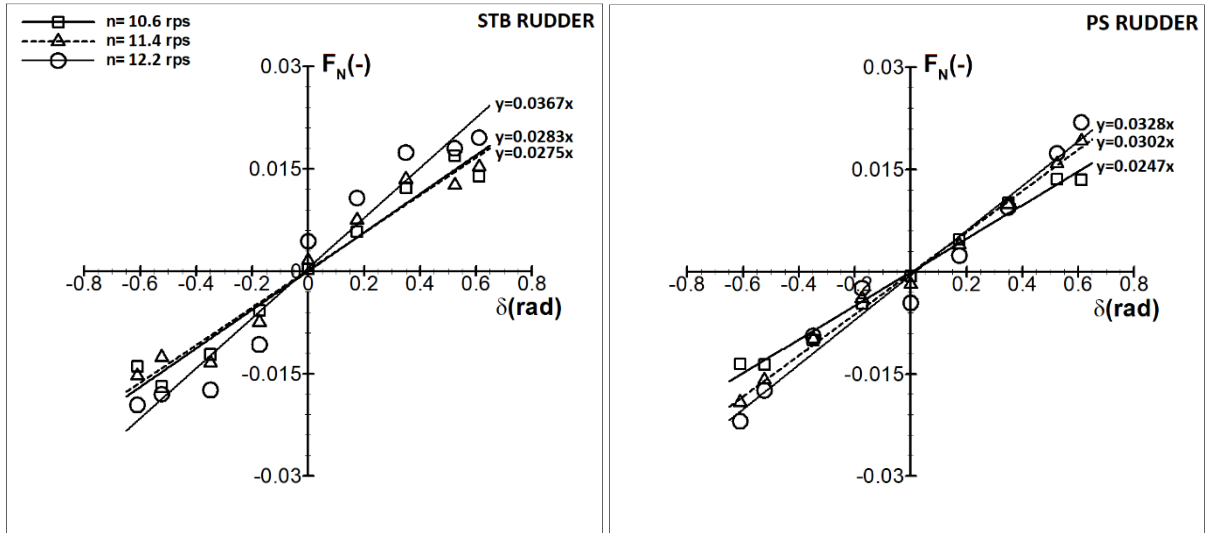


Fig. 11.  $F_N^{P,S}$  values in straight motion for rudder angles under different propeller loads.

In order to calculate the rudder normal force ( $F_N$ ) given in Eqn.9 , longitudinal and lateral components of the rudder inflow velocity has to be determined. In Eqn.13, wake fraction ratio at propeller plane and rudder ( $\varepsilon$ ) and the experimental constant ( $\kappa$ ) are the unknowns that need to be estimated. These values can be predicted from the static rudder tests under various propeller loads. Fig.11 shows the results of static drift simulations under various propeller loads. The symbols present the predicted values by CFD, while the lines indicate the linear fitting curves to computed values. The coefficients  $\varepsilon$  and  $\kappa$  are obtained using the slopes of  $F_N$ - $\delta$  curves at  $\delta = 0$  for both rudders shown in Figure 11 and the relation between  $u'_R/u'_P$  and  $\sqrt{1 + 8K_T/\pi J_P^2} - 1$  shown in Figure 12. Subsequently, the procedure presented by Yasukawa and Yoshimura (2015) is followed here to calculate  $u'_R$ .

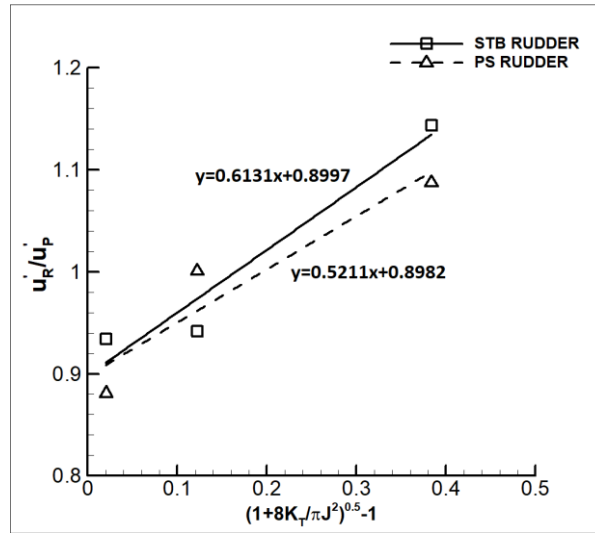
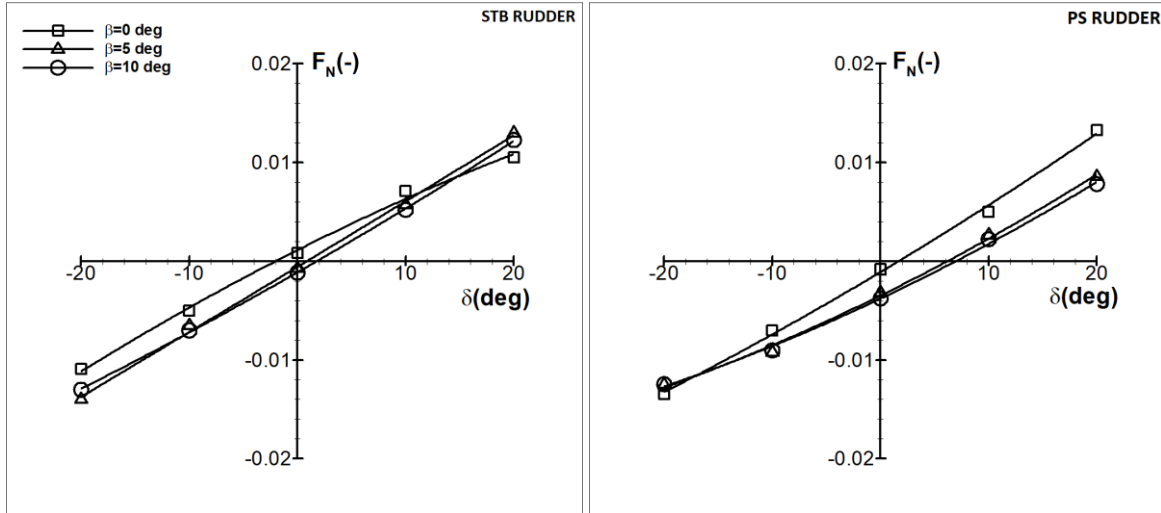


Fig. 12. Ratio of the inflow velocities of rudder and propeller at different propeller loads.

Utilizing the relation between  $u'_R/u'_P$  and  $\sqrt{1 + 8K_T/\pi J_P^2} - 1$  as shown in Figure 12, Eqn.13 can be solved. The ratio of propeller diameter to rudder span is taken as  $\eta = 1.3457$ . As a result,  $\varepsilon$  and  $\kappa$  are determined as 0.89 and 0.50 for the port side rudder, and 0.90 and 0.59 for the rudder at starboard side, respectively.

The flow straightening factor due to sway velocity,  $\gamma_R$ , is determined separately for the port and starboard rudders from the drift-rudder simulations, while the flow straightening factor due to the yaw rate of ship is assumed as  $l'_R = 2\chi'_R$ . Although it is shown that the coefficients  $\gamma_R$  and  $l'_R$  are slightly

asymmetric for the port and starboard turnings for TPTR ships (Kang et al., 2008), they are assumed to be symmetrical in this study. According to Eqn.11 given for TPTR ships (Khanfir et al, 2011), the effective rudder angles ( $\delta_R^{P,S}$ ) at which the rudder normal force equals to zero, should be obtained at different drift angles. Initially, the rudder normal forces versus various rudder angles are curve fitted for different drift angles. Subsequently, the rudder angles which return zero rudder normal force are determined from the fitted curves for both rudders. It is obvious from Figure 13 that the rudder normal force has different tendency for the port and starboard rudders. The variation in the rudder normal force shows that there is an asymmetric flow on the rudders in maneuvering motions for TPTR ships. Finally, the effective rudder angles versus various drift angle are fitted with the linear curves, and the slope of the fitted curves give the  $\gamma_R^{P,S}$ .



**Fig. 13.** Rudder normal force for varying rudder angles at different drift simulation.

In Figure 14, only the effective rudder angles ( $\delta_R^{P,S}$ ) in starboard side during maneuvering are shown and  $\beta_R$  given in Eqn.12 is taken as  $\beta$  since the yaw rate ( $r'$ ) of the ship is zero for drift-rudder simulations. In this study, it is presumed that  $\delta_R^S$  in the starboard side maneuvering ( $\beta > 0$ ) is equal to  $-\delta_R^P$  in the port side maneuvering, where a similar assumption was made in the study of Kim et al. (2007) for a TPTR ship. It is also noted that the same assumption is made for the coefficient  $\gamma_R$  in maneuvering motions. Consequently, all parameters computed from the static rudder and drift-rudder simulations for the prediction of rudder force are given in Table 13. It is worthy note here that  $\varepsilon$  and  $\kappa$  values of rudders are different for port and starboard sides. It is normal for rudders of a TPTR ship to have different values because of the asymmetric incoming flow (Umeda et al., 2014).

**Table 13.** Parameters obtained by CFD for calculating the rudder forces in maneuvering motions.

Parameters	Rudder (Starboard)	Rudder (Port)
$a_H$	0.0858	0.0858
$t_R$	0.4404	0.4404
$x'_H$	-0.4371	-0.4371
$\varepsilon$	0.90	0.89
$\kappa$	0.59	0.50
$\gamma_R (\beta_R < 0)$	0.5317	0.3713
$\gamma_R (\beta_R > 0)$	0.3713	0.5317
$l'_R$	-0.9436	-0.9436

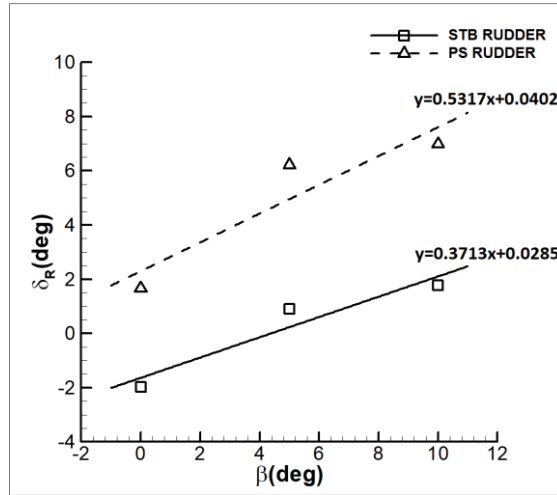


**Fig. 14.** The effective rudder angles where the rudder normal force is zero at different drift angles.

#### 5.4 Hydrodynamic Derivatives

In order to obtain the resistance coefficient  $X_0$ , and sway-velocity dependent hydrodynamic derivatives such as  $Y_v, N_v, X_{vv}, Y_{vvv}, N_{vvv}$ , the forces and moment obtained from the static drift simulations are curve fitted to polynomial functions by the least square method as shown in Eqn.15. The predicted derivatives are compared with the published CFD results (Sakamoto et al., 2012) and the EFD data (Yoon, 2009), as listed in Table 14. The linear derivatives are predicted numerically closer to measured data compared to higher order derivatives, which are generally difficult to estimate accurately. However, it can still be stated that all derivatives by the present CFD are in a good agreement with (Sakamoto et al., 2012) and (Yoon, 2009).

**Table 14.** Comparison of the hydrodynamic derivatives obtained from the static drift test.

Hydrodynamic Derivatives	Fr = 0.280			
	Present CFD	CFD-Sakamoto	EFD-Yoon	E%D
$X'_0$	-0.0161	-	-0.0170	-5.3
$X'_{vv}$	-0.1823	-0.1480	-0.1528	19.3
$Y'_v$	-0.2937	-0.3120	-0.2961	-0.9
$Y'_{vvv}$	-1.1735	-1.5370	-1.9456	-39.7
$N'_v$	-0.1622	-0.1510	-0.1667	-2.7
$N'_{vvv}$	-0.2252	-0.2340	-0.4355	-48.3

For the pure yaw and yaw-drift simulations, the hydrodynamic derivatives are obtained by analyzing the time histories of forces and moment using the Fourier series (FS) method which is suitable for the motions prescribed by sine and cosine functions. FS coefficients are obtained using the formula given in Eqn.19. In this study, low order 'Single-Run (SR)' and 'Multiple-Run (MR<sub>L</sub>)' (Yoon et al., 2015) approaches are used to evaluate the hydrodynamic derivatives and the effects of these two methods on turning and zigzag maneuvers are compared with each other. In the former method (SR), there is no need to fit a function to determined FS coefficients, thus the derivatives can be calculated algebraically. The latter includes quadratic or cubic functions to be fitted to the FS coefficients with respect to the parameters of interest such as  $v'_{max}, r'_{max}$ . By using the expressions given in Table 6 for the MR<sub>L</sub> method, the yaw-rate dependent and cross-coupled hydrodynamic derivatives are obtained and compared with the numerical (Sakamoto et al., 2012) and experimental (Yoon et al., 2015) results, as listed in Table 15. Here, it should be noted that the pure yaw simulations by Sakamoto et al., 2012 are performed up to  $r'_{max} = 0.60$ , whereas the results given for the present study and experimental

data are obtained up to  $r'_{max} = 0.75$ . All cross-coupled derivatives given in Table 15 are determined at a constant yaw rate ( $r'_{max} = 0.30$ ) with  $\beta = 9^\circ, 10^\circ, 11^\circ$ . Moreover, the ratios of hydrodynamic derivatives by SR method to  $MR_L$  method are shown in Figure 15. A ratio of 1 between SR and  $MR_L$  presents compatible agreement. In terms of linear rotary derivatives ( $Y'_r, N'_r$ ) SR method is close to  $MR_L$  method. However this is not the case for the non-linear ones,  $X'_{rr}$  and  $Y'_{rrr}$ , especially at the smallest  $r'_{max}$  value, the ratio of the derivatives nearly go up to 20. It can also be deduced from Figure 15 that the cross-coupled derivatives by the SR method agree well with those of  $MR_L$  for all  $\beta$  values except for the values of  $N'_{vrr}$ .

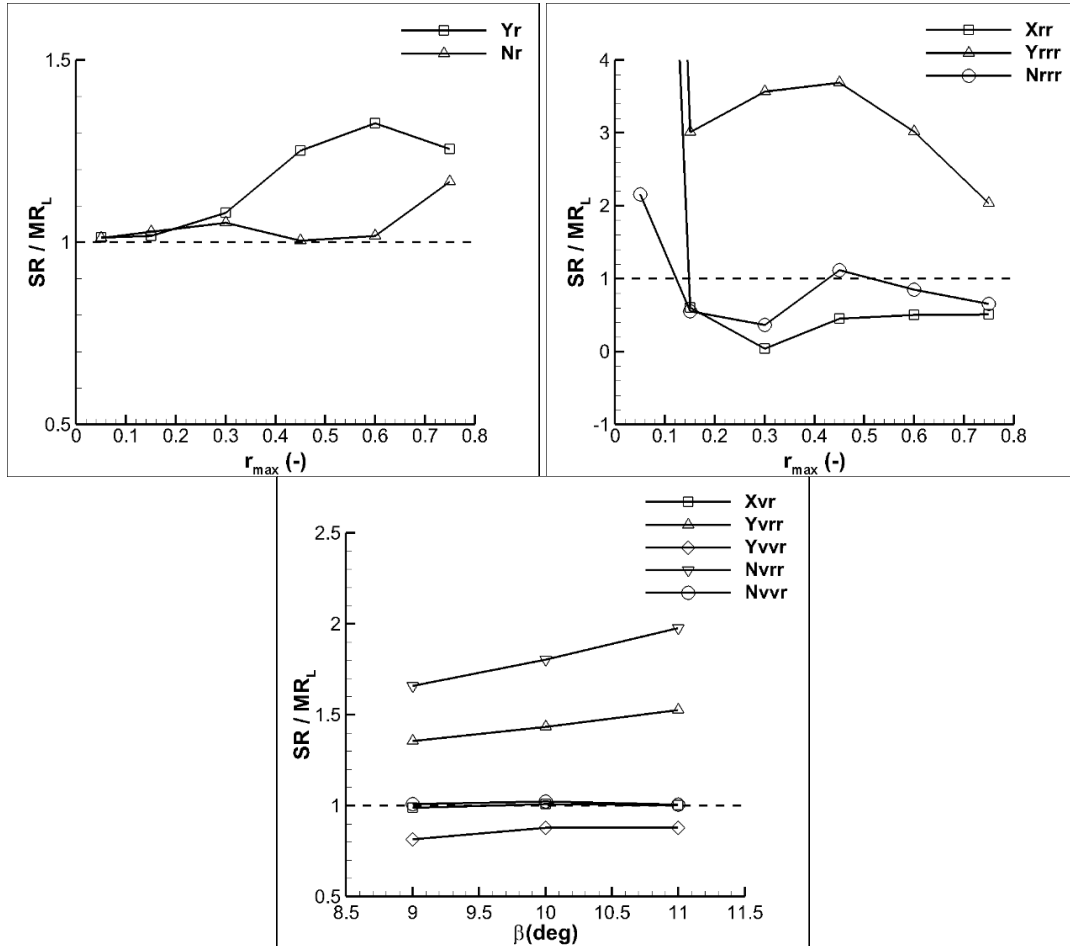


**Fig. 15.** Ratio of hydrodynamic derivatives predicted by SR and  $MR_L$  methods. (A ratio of 1 between SR and  $MR_L$  presents compatible agreement.)

**Table 15.** Comparison of hydrodynamic derivatives obtained from pure yaw and yaw-drift tests by  $MR_L$  method.

Hydrodynamic Derivatives	Fr = 0.280			E%D
	Present	CFD-Sakamoto	EFD-Yoon	
$X'_{rr} + m'x'_G$	-0.0280	-0.0293	-0.0282	-0.7
$Y'_r - m' - m'_x$	-0.0536	-0.0420	-0.0485	10.5
$Y'_{rrr}$	-0.0519	-0.0190	-0.0452	14.8
$N'_r - m'x'_G$	-0.0439	-0.0420	-0.0485	-9.5
$N'_{rrr}$	-0.0479	-0.0320	-0.0505	-5.1
$X'_{vr} + m' + m'_y$	0.0152	-0.0953	0.0819	-83.4
$Y'_{vrr}$	-0.7844	-39.9200	-2.0198	-57.9
$Y'_{vvr}$	-1.5063	-1.6140	-1.8819	-28.4
$N'_{vrr}$	-0.2177	-7.6473	-0.6891	-74.5
$N'_{vvr}$	-0.7997	-0.3995	-0.4367	72.6

## 5.5 Maneuvering Simulations

Maneuvering performance of the ship is evaluated by selecting  $-35^\circ$  turning and  $-20^\circ/-20^\circ$  zigzag tests to verify the validity of the maneuvering coefficients determined by both SR and MR<sub>L</sub> methods. Since the hydrodynamic derivatives calculated by the SR method can be obtained at more than one  $r'_{max}$  and  $\beta$  values, the turning and zigzag maneuvers are simulated using the SR combinations shown in Table 16. Note that the hydrodynamic derivatives computed from the static drift test are kept constant in the combinations generated, whereas only the values of derivatives obtained from the dynamic tests alter according to the  $r'_{max}$  and  $\beta$  values. The free maneuvering simulations are performed using a 3-DOF MMG mathematical model proposed by Yasukawa and Yoshimura (2015).

**Table 16.** SR combinations used in the turning and zigzag maneuvers.

	$\beta = 9^\circ, r'_{max} = 0.30$	$\beta = 10^\circ, r'_{max} = 0.30$	$\beta = 11^\circ, r'_{max} = 0.30$
$r'_{max} = 0.05$	SR <sub>1</sub>	SR <sub>7</sub>	SR <sub>13</sub>
$r'_{max} = 0.15$	SR <sub>2</sub>	SR <sub>8</sub>	SR <sub>14</sub>
$r'_{max} = 0.30$	SR <sub>3</sub>	SR <sub>9</sub>	SR <sub>15</sub>
$r'_{max} = 0.45$	SR <sub>4</sub>	SR <sub>10</sub>	SR <sub>16</sub>
$r'_{max} = 0.60$	SR <sub>5</sub>	SR <sub>11</sub>	SR <sub>17</sub>
$r'_{max} = 0.75$	SR <sub>6</sub>	SR <sub>12</sub>	SR <sub>18</sub>

Derivatives by SR and MR<sub>L</sub> methods are tested in an in-house code (MANSIM) that utilizes the MMG mathematical model. In order to determine which SR combination gives the closest results to EFD data in the turning maneuver, the average absolute deviation of parameters such as advance ( $A'_T$ ), transfer ( $T'_T$ ), tactical diameter ( $TD'_T$ ), diameter in steady turn ( $D'_T$ ), steady yaw rate ( $r'_T$ ) and steady turning speed ( $U'_T$ ) are taken into consideration. In addition, the average absolute deviation of first and second overshoot angles ( $OA_{1st}, OA_{2nd}$ ) are calculated for the zigzag maneuver. The comparison of the results by using 12 different SR combinations and MR<sub>L</sub> method is shown in Figure 16. Some combinations are not shown in Figure 16 as they failed to resolve the equations of motion due to inaccurate prediction of the hull forces and moment, thus they did not give reasonable results. When the average deviations are compared, it can be seen that SR4 which includes the derivatives from the pure yaw analysis with  $r'_{max} = 0.45$  and yaw-drift analysis with minimum  $\beta$  value gives the closest result to the EFD data. It can also be stated that the average deviations for both results of SR and MR<sub>L</sub> are getting smaller as  $\beta$  value in the yaw-drift simulations decreases.

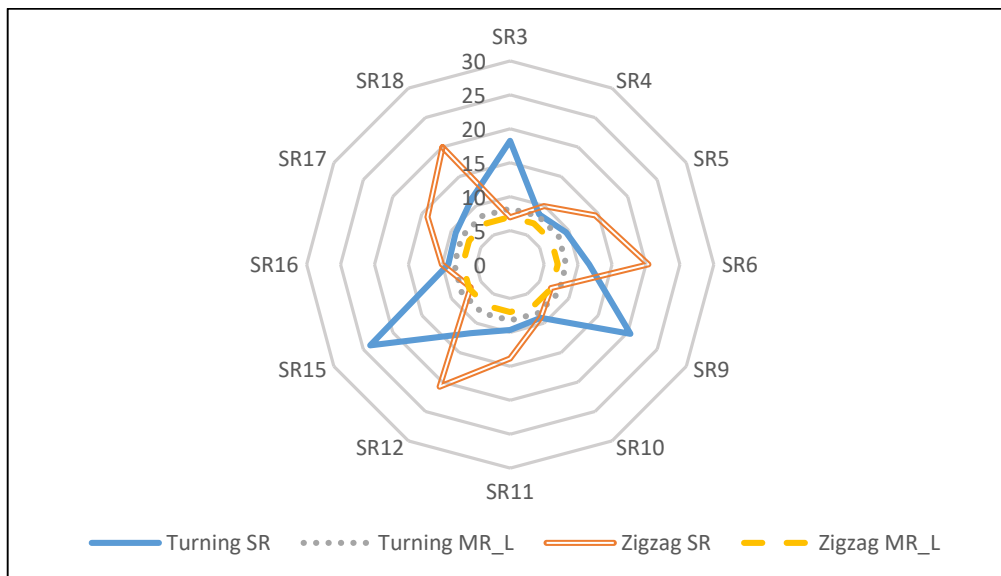


**Fig. 16.** Average absolute deviations ( $\bar{E}\%D$ ) for turning and zigzag tests by SR and MR<sub>L</sub> methods.

After finding the best option in combinations from Figure 16, the hydrodynamic derivatives from SR4 combination are used to generate turning and zigzag maneuvers and compared the average relative errors of maneuvering indices with those of MR<sub>L</sub>. The Euler algorithm is applied to simulate the maneuvers and time step is set to be  $h = 0.1s$ . The rudder is deflected with a constant deflection rate of  $9^\circ/s$  as in the experiment until the maximum rudder angle is reached. Figure 17 shows the comparison of predicted turning trajectory and time histories of the kinematical parameters ( $r$ ,  $U$ ,  $\beta$ ) with the free running data from MARIN at  $Fr = 0.25$  in full scale. Although both methods (SR and MR<sub>L</sub>) slightly overestimate the turning trajectory with respect to free-running data, the turning trajectory and other kinematical parameters obtained by the SR method agree well with the MR<sub>L</sub> results.

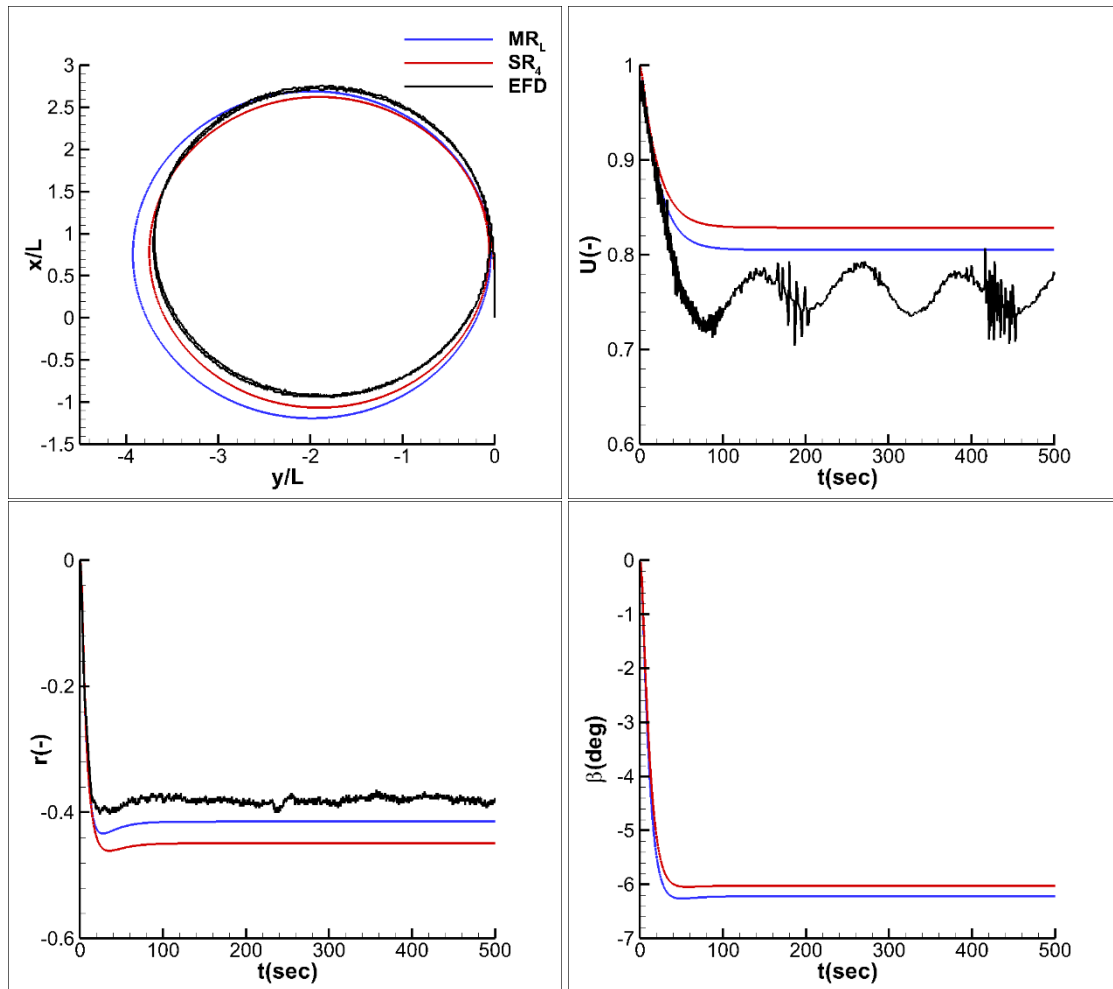


**Fig. 17.** Comparison of predicted trajectories and kinematic parameters of turning maneuver with MARIN free running data.

**Table 17.** Comparison of the predicted turning indices with MARIN free running data.

	<i>EFD</i>	<i>MR<sub>L</sub></i>	<i>SR<sub>4</sub></i>	<i>Empirical</i>	<i>E<sub>MR</sub>%D</i>	<i>E<sub>SR</sub>%D</i>
$A'_T$	2.71	2.67	2.61	2.55	-1.5	-3.7
$T'_T$	1.46	1.78	1.72	1.15	21.9	17.8
$TD'_T$	3.65	3.92	3.74	2.83	7.9	2.4
$D'_T$	3.66	3.91	3.69	2.69	6.9	0.8
$r'_T$	-0.38	-0.41	-0.44	-	5.2	15.6
$U'_T$	0.75	0.80	0.83	0.62	6.7	10.7
$ \bar{E}  \% D$					<b>8.3</b>	<b>8.5</b>

The comparison of turning indices are shown in Table 17. Reasonable agreement is achieved for the  $MR_L$  method with an average deviation of 8.3% ,and the best SR method (see Fig. 16) capture the free running data with an average deviation of 8.5%. Table 17 also covers results obtained by empirical equations stated for twin propeller ships by (Lyster and Knights; 1979). Investigating all the results given in the table, it might be stated that the empirical relations provided by (Lyster and Knights; 1979) can be a good alternative for primary calculations of ship maneuvering.

Figure 18 and Table 18 depicts the comparison of results predicted by  $SR_4$  and  $MR_L$  methods with the free running data of zigzag maneuver, where the heading and rudder angles, and the trajectories are shown. The rudder period in the first cycle is captured well by both SR and  $MR_L$  methods, however the difference in the second cycle with the free running data, leading to a phase difference for the heading angle and the trajectory. On the whole, the results obtained in the turning and zigzag maneuver by SR method presented almost the same level of magnitude with the  $MR_L$  method when appropriate PMM conditions are adopted.

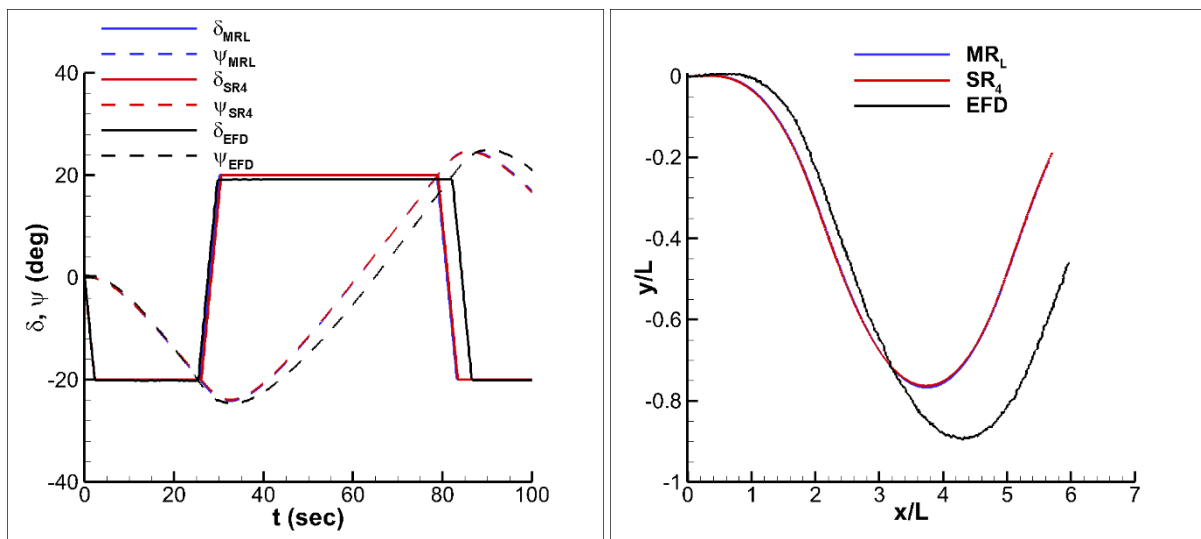


**Fig. 18.** Comparison of the trajectories and kinematic parameters of zigzag maneuver with the MARIN free running data.

**Table 18.** Comparison of the predicted zigzag indices with MARIN free running data.

	<i>EFD</i>	<i>MR<sub>L</sub></i>	<i>SR<sub>4</sub></i>	<i>E<sub>MR</sub>%D</i>	<i>E<sub>SR</sub>%D</i>
<i>OA<sub>1st</sub></i> (deg)	4.70	4.15	3.94	-11.7	-16.2
<i>OA<sub>2nd</sub></i> (deg)	4.80	4.69	4.62	-2.3	-3.8
$ \bar{E}  \%D$				<b>7.0</b>	<b>10.0</b>

## 6. Conclusions

In this study, maneuvering performance of a twin-propeller and twin-rudder ship was numerically simulated. A modular MMG mathematical model was implemented. Static drift, pure yaw, yaw and drift and rudder tests were numerically carried out for DTMB 5415 surface combatant at  $Fr = 0.28$  utilizing a RANSE based CFD solver. Self-propulsion point of the ship was calculated by numerical self-propulsion tests to obtain the rotation rate of the propeller during maneuvering at  $Fr = 0.25$ .

Results of the present study agree well with experimental and another numerical result found in the literature for static drift and PMM tests. Propeller forces were calculated by numerical self-propulsion tests and rudder forces by simulating static rudder and combined rudder- drift tests. These

forces can implicitly be validated by comparing the turning circle and zigzag maneuvers obtained either by experiments or by CFD-based methods. However; due to the nature of system-based methods such as the one adopted in this paper, additional validations regarding the propeller and rudder should be made.

Hydrodynamic derivatives from PMM tests were obtained by two different methods; the single-run method and the multiple-run method. It was found out that the derivatives obtained by the single-run method generate the turning and zigzag maneuvering motions very close to that generated by the low-order multiple-run method. From the practical point of view, hydrodynamic derivatives can be determined with SR method by performing only one CFD simulation, providing an advantage in terms of computational time. However, performance of the single-run method was not satisfactory for all PMM test conditions in the maneuvering tests. If single-run method is to be used; then special attention must be paid when selecting the PMM test conditions. Similar studies are planned as future studies for other benchmark ships to validate the findings of this study.

## References

- [1] K. Kijima, T. Katsuno, Y. Nakiri, Y. Furukawa, On the maneuvering performance of a ship with the parameter of loading condition, *J. Soc. Nav. Archit. Jpn.* 168 (November) (1990) 141–148.
- [2] H.Y. Lee, S.S. Shin, The prediction of ship's manoeuvring performance in initial design stage, *Practical Design of Ships and Mobile Units* (1998) 633–639.
- [3] Y. Yoshimura and Y. Masumoto, Hydrodynamic database and manoeuvring prediction method with medium high-speed merchant ships and fishing vessels, *Journal of the Japan Society of Naval Architects and Ocean Engineers*, 14 (2011) 63-73.
- [4] J. Liu, R. Hekkenberg, F. Quadvlieg, H. Hopman, B. Zhao, An integrated empirical manoeuvring model for inland vessels. *Ocean Engineering* 137 (2017) 287-308.
- [5] Z. Shen, D. Wan, P. M. Carrica, Dynamic overset grids in OpenFOAM with application to KCS self-propulsion and maneuvering, *Ocean Engineering* 108 (2015) 287-306.
- [6] P. M. Carrica, A. Mofidi, K. Eloit, G. Deflortrie, Direct simulation and experimental study of zigzag maneuver of KCS in shallow water, *Ocean Engineering* 112 (2016) 117-133.
- [7] K. Ohashi, H. Kobayashi, T. Hino, Numerical simulation of the free-running of a ship using the propeller model and dynamic overset grid method, *Ship Technology Research* (2018) 1-10.
- [8] P. M. Carrica, F. Ismail, M. Hyman, S. Bhushan, F. Stern, Turn and zigzag maneuvers of a surface combatant using a URANS approach with dynamic overset grids, *Journal of Marine Science and Technology* 18.2 (2013) 166-181.
- [9] O. E. Moctar, U. Lantermann, P. Mucha, J. Hopken, T. E. Schellin, RANS-based simulated ship maneuvering accounting for hull-propulsor-engine interaction, *Ship Technology Research* 61.3 (2014) 142-161.
- [10] G. Dubbioso, D. Durante, A. Di Mascio, R. Broglia, Turning ability analysis of a fully appended twin screw vessel by CFD. Part II: Single vs. twin rudder configuration, *Ocean Engineering* 117 (2016) 259-271.
- [11] N. Sakamoto, P.M. Carrica, F. Stern, URANS simulations of static and dynamic maneuvering for surface combatant: part 1. Verification and validation for forces, moment, and hydrodynamic derivatives, *Journal of Marine Science and Technology* 17.4 (2012a) 422-445.
- [12] H. Yoon, C.D. Simonsen, L. Benedetti, J. Longo, Y. Toda, F. Stern, Benchmark CFD validation data for surface combatant 5415 in PMM maneuvers—Part I: Force/moment/motion measurements, *Ocean Engineering* 109 (2015a) 705-734.

- [13] Y. Liu, L. Zou, Z. Zou, H. Guo, Predictions of ship maneuverability based on virtual captive model tests, *Engineering Applications of Computational Fluid Mechanics* 12.1 (2018) 334-353.
- [14] M. A. Abkowitz, *Lectures on ship hydrodynamics steering and manoeuvrability*, Lyngby: Hydro- and Aerodynamics Lab (1964).
- [15] A. Ogawa, H. Kasai, On the mathematical method of manoeuvring motion of ships, *Int. Shipbuilding Progress* 25(292) (1978) 306–319.
- [16] H. Yasukawa, Y. Yoshimura, Introduction of MMG standard method for ship maneuvering predictions, *Journal of Marine Science and Technology* 20.1 (2015) 37-52.
- [17] J. Liu, F. Quadvlieg, R. Hekkenberg, Impacts of the rudder profile on manoeuvring performance of ships, *Ocean Engineering* 124 (2016) 226-240.
- [18] S. He, P. Kellett, Z. Yuan, A. Incecik, O. Turan, E. Boulougouris, Manoeuvring prediction based on CFD generated derivatives. *Journal of Hydrodynamics*, 28(2) (2016) 284-292.
- [19] D. Kang, V. Nagarajan, K. Hasegawa, M. Sano, Mathematical model of single-propeller twin-rudder ship, *Journal of Marine Science and Technology*, 13(3) (2008) 207-222.
- [20] S. K. Lee, M Fujino, Assessment of a Mathematical Model for the Manoeuvring Motion of a Twin-Propeller Twin-Rudder Ship, *International Shipbuilding Progress* 50.1, 2 (2003) 109-123.
- [21] S. Khanfir, K. Hasegawa, V. Nagarajan, K. Shouji, S. K. Lee, Manoeuvring characteristics of twin-rudder systems: rudder-hull interaction effect on the manoeuvrability of twin-rudder ships, *Journal of Marine Science and Technology*, 16(4) (2011) 472-490.
- [22] H. P. Guo, Z. J. Zou, Y. Liu, F. Wang, Investigation on hull-propeller-rudder interaction by RANS simulation of captive model tests for a twin-screw ship, *Ocean Engineering*, 162 (2018) 259-273.
- [23] H. Guo, Z. Zou, System-based investigation on 4-DOF ship maneuvering with hydrodynamic derivatives determined by RANS simulation of captive model tests, *Applied Ocean Research* 68 (2017) 11-25.
- [24] S. Motora, On the measurement of added mass and added moments of inertia for ship motions (in Japanese), *J. Soc. Nav. Archit. Jpn.* 105 (1959) 83–89.
- [25] S. Motora, On the measurement of added mass and added moments of inertia for ship motions, Part 2: added mass for the longitudinal motions (in Japanese), *J. Soc. Nav. Archit. Jpn.* 106 (1960a) 59–62.
- [26] S. Motora, On the measurement of added mass and added moments of inertia for ship motions, Part 3: added mass for the transverse motions (in Japanese), *J. Soc. Nav. Archit. Jpn.* 106 (1960b) 63–68.
- [27] S. Inoue, M. Hirano, K. Kijima, J. Takashina, A practical calculation method of ship maneuvering motion, *International Shipbuilding Progress* 28 325 (1981) 207-222.
- [28] Y. G. Kim, S. Y. Kim, H. T. Kim, S.W. Lee, B. S. Yu, Prediction of the maneuverability of a large container ship with twin propellers and twin rudders, *Journal of Marine Science and Technology* 12 3 (2007) 130-138.
- [29] S. Bhushan, T. Xing, P. M. Carrica, F. Stern, Model-and full-scale URANS simulations of Athena resistance, powering, seakeeping, and 5415 maneuvering, *Journal of Ship Research* 53 4 (2009) 179-198.
- [30] N. Sakamoto, P. M. Carrica, F. Stern, URANS simulations of static and dynamic maneuvering for surface combatant: part 2. Analysis and validation for local flow characteristics, *Journal of Marine Science and Technology* 17 4 (2012b) 446-468.
- [31] H. Yoon, J. Longo, Y. Toda, F. Stern, Benchmark CFD validation data for surface combatant 5415 in PMM maneuvers—Part II: Phase-averaged stereoscopic PIV flow field measurements, *Ocean Engineering* 109 (2015b) 735-750.

- [32] M. O. Woolliscroft, K. J. Maki, A fast-running CFD formulation for unsteady ship maneuvering performance prediction, *Ocean Engineering* 117 (2016) 154-162.
- [33] H. Yoon, Phase-averaged stereo-PIV flow field and force/moment/motion measurements for surface combatant in PMM maneuvers, PhD thesis, The University of Iowa (2009).
- [34] F. R. Menter, Two-equation eddy-viscosity turbulence models for engineering applications, *AIAA Journal* 32 8 (1994) 1598-1605.
- [35] F. Stern, R. V. Wilson, H. V. Coleman, E. G. Paterson, Comprehensive approach to verification and validation of CFD simulations—part 1: methodology and procedures, *Journal of Fluids Engineering* 123 4 (2001) 793-802.
- [36] C. D. Simonsen, J. F. Otzen, C. Klimt, N. L. Larsen, F. Stern, Maneuvering predictions in the early design phase using CFD generated PMM data, 29th Symposium on Naval Hydrodynamics (2012).
- [37] T. Xing, S. Bhushan, F. Stern, Vortical and turbulent structures for KVLCC2 at drift angle 0, 12, and 30 degrees, *Ocean Engineering* 55 (2012) 23-43.
- [38] M. Falchi, M. Felli, S. Grizzi, G. Aloisio, R. Broglio, F. Stern, SPIV measurements around the DELFT 372 catamaran in steady drift, *Experiments in Fluids* 55 11 (2014) 1844.
- [39] R. R. Shenoi, P. Krishnankutty, R. P. Selvam, Study of manoeuvrability of container ship by static and dynamic simulations using a RANSE-based solver, *Ships and Offshore Structures* 11 3 (2016) 316-334.
- [40] Z. Zhou, S. Yan, W. Feng, Manoeuvring prediction of multiple-purpose cargo ships (in Chinese), *Ship Eng.* 6 (1983) 21–36.
- [41] D. Clarke, P. Gedling, G. Hine, Application of manoeuvring criteria in hull design using linear theory, *Trans. R. Inst. Nav. Archit.* 125 (1983) 45–68.
- [42] S. Duman, S. Bal, Prediction of the turning and zig-zag maneuvering performance of a surface combatant with URANS, *Ocean Systems Engineering, An International Journal*, 7 4 (2017) 435-460.
- [43] S. Duman, F. Cakici, S. Bal, Numerical Simulation of Dynamic Maneuvering of a Surface Combatant Using Overset Grid Method, *Proc. 3rd International Symposium on Naval Architecture and Maritime (INT-NAM 2018)*, April 24-25 (2018) 643-655.
- [44] O.F. Sukas, O.K. Kinaci, S. Bal, A Review on Prediction of Ship Manoeuvring Performance-Part 1 (in Turkish), *GMO Journal of Ship and Marine Technology*, The Turkish Chamber of Naval Architects and Marine Engineers, 210 December (2017) 37-75.
- [45] O.F. Sukas, O.K. Kinaci, S. Bal, A Review on Prediction of Ship Manoeuvring Performance-Part 2 (in Turkish), *GMO Journal of Ship and Marine Technology*, The Turkish Chamber of Naval Architects and Marine Engineers, 210 December (2017) 76-106.
- [46] M. Vantorre, Review of practical methods for assessing shallow and restricted water effects, *International Conference on Marine Simulation and Ship Maneuverability (MARSIM'03)* (2003).
- [47] J. Liu, R. Hekkenberg, Sixty years of research on ship rudders: effects of design choices on rudder performance, *Ships and Offshore Structures*, 12 4 (2017) 495-512.
- [48] J. Liu, R. Hekkenberg, E. Rotteveel, H. Hopman, Literature review on evaluation and prediction methods of inland vessel manoeuvrability, *Ocean Engineering* 106 (2015) 458-471.
- [49] S. Sutulo, C. G. Soares, Mathematical models for simulation of manoeuvring performance of ships, *Marine Technology and Engineering* (2011) 661-698.
- [50] O. K. Kinaci, O. F. Sukas, S. Bal, Prediction of wave resistance by a Reynolds-averaged Navier-Stokes equation-based computational fluid dynamics approach, *Journal of Engineering for the Maritime Environment*, 230 3 (2016) 531-548.
- [51] ITTC – Recommended Procedures and Guidelines. 7.5-02 03-01.4 rev. 3, 1978 ITTC Performance Prediction Method, (2014).

- [52] H. Yoon, L. Gui, S. Bhushan, F. Stern, Tomographic PIV Measurements For Surface Combatant 5415 Straight Ahead and Static Drift 10 and 20 Degree Conditions, 30th Symposium on Naval Hydrodynamics, Hobart, Tasmania, Australia, (2014).
- [53] C. A. Lyster, H. L. Knights, Prediction Equations for Ships' Turning Circles. *Trans. NECIES*, 95, (1979) 217-232.
- [54] ITTC – Recommended Procedures and Guidelines. 7.5-02 06-02 rev. 5, Captive Model Test Procedure (2017).
- [55] M. Araki, H. S. Hosseini, Y. Sanada, K. Tanimoto, N. Umeda, F. Stern, Estimating maneuvering coefficients using system identification methods with experimental, system-based, and CFD free-running trial data, *Ocean engineering* 51 (2012) 63-84.
- [56] Y. Arai, T. Hino, CFD simulations of PMM test using local grid refinement with an overset grid method, *Journal of The Japan Society of Naval Architects and Ocean Engineers* 25 (2016) 77-91 (in Japanese).
- [57] N. Umeda, T. Furukawa, A. Matsuda, S. Usada, Rudder normal force during broaching of a ship in stern quartering waves. In: *Proceedings of the 30th ONR Symposium on Naval Hydrodynamics*, Tasmania, Australia, (2014).